Stochastic analysis of locally resonant linear and hysteretic metamaterials for seismic isolation of process equipment

Oreste S. Bursi[1], Francesco Basone[1,2], Moritz Wenzel[1]

[1] Department of Civil, Environmental and Mechanical Engineering, University of Trento, Via Mesiano 77, 38123 Trento, Italy
[2] Engineering and Architecture Faculty, University of Enna "Kore", Viale delle Olimpiadi, 94100 Enna, Italy

Correspondence: Oreste S. Bursi, Department of Civil, Environmental and Mechanical Engineering, University of Trento, Trento, Italy. Email: oreste.bursi@unitn.it

Abstract

Periodic metafoundations have proven to inherit valuable properties from wave propagating in phononic periodic structures in the very low-frequency regime. Therefore, finite locally resonant metafoundations (LRMs) represent a novel type of seismic isolation for ultralow-frequency applications. In this context, it is still unknown the impact that massive resonators with varying frequencies or devices with hysteretic behavior can entail on the whole system performance. For this purpose, we develop and optimize two finite locally resonant multiple degrees of freedom (MDoF) metafoundations in this paper: i) a foundation endowed with resonators, linear springs and linear viscous dampers tuned to multiple frequencies; and ii) a foundation equipped with fully nonlinear hysteretic dampers. Both are optimized considering the stochastic nature of ground motion, modelled with a modified Kanai-Tajimi filter in the stationary frequency domain, and a massive MDoF superstructure, chosen to be a fuel storage tank. In order to take all of the above-mentioned effects into account, we establish a procedure based on nonlinear programming that is able to optimize any number of parameters. More precisely, to optimize the nonlinear behavior of damper devices we employ a Bouc-Wen hysteretic model. Therefore, we reduce the nonlinear differential equations of Bouc-Wen models to a system of linear equations through the stochastic (equivalent) linearization technique. Moreover, we test the optimized systems against natural seismic records both with linear and nonlinear time history analyses. To investigate the role of hysteresis on the nonlinear band structure, we derive linearized and nonlinear dispersion relationships for the uncoupled periodic metafoundation. Finally, we obtain further detailed information on the nonlinear wave propagation by means of spectro-spatial analysis.

Keywords

Phononic periodic structures, finite locally resonant metafoundations, ultralow-frequency domain, nonlinear programming, equivalent linearization technique.

1. Introduction

1.1 Background and motivations

Applied research in phononic periodic materials and structures has been abundant in recent years especially in the mid-frequency regime. See among others, the dense state of art of Hussein et al. [1], the investigation in acoustic metamaterials [2], the review of waves behavior in structured mediums [3] and the relevant problems of optimization. Investigations in the field of solid-state physics have shown that certain crystal arrangements may be used to manipulate the energy or patterns of acoustic (mechanical) wave energy [4-8]. These elastic materials, termed phononic crystals, can be designed to produce specific gaps in the frequency response of the structure. More precisely, when the frequency contents of a wave fall within the range of the frequency band gap of a periodic structure, the wave, and its energy, cannot propagate because they become evanescent. While acoustic/elastic metamaterials have provided a root to subwavelength applications, it is still challenging to control and attenuate waves in the ultralow-frequency domain.

Within linear metamaterials, a new category of applications of phononic – or periodic - structures as alternative to classical seismic isolators to earthquake mitigation has received growing interest [9-11]. Their increasing popularity resides in the possibility of exploiting the advantages of periodic structures that are able to attenuate waves in certain frequency ranges. In particular, the authors exploit the advantages of LRMs, due to their capability of attenuating low-frequency waves by means of unit cells much smaller than the wavelength of the desired frequency region. In fact, the most common solutions of isolation use lead-rubber bearings or spherical bearing devices. Although they are quite effective for the horizontal components of earthquakes, they require two strong floors, exert a very high stiffness against the vertical component of an earthquake, and seem to be ineffective for large structures subjected to rocking [12]. In order to reduce the seismic response of a superstructure, Casablanca et al. studied periodic and finite LRM foundations [13]. Although good results were obtained in terms of response reduction, neither of the proposed periodic systems were designed for gravity and/or seismic load combinations. Furthermore, the authors did not take into account the feedback forces from superstructures to metafoundations.

In order to overcome these drawbacks, other researchers [14-15] proposed a finite lattice LRM, the so-called Metafoundation, for the seismic protection of process equipment, e.g. storage tanks. The foundation consists of standard steel columns and concrete slabs that define the primary load bearing structure, while massive concrete masses are considered as resonators. Moreover, the foundation was designed to remain undamaged for safe shutdown earthquakes (SSEs). In order to evaluate the optimal parameters of the resonators and to account for the stochastic nature of seismic waves, the authors proposed an optimization procedure based on nonlinear programming in the frequency domain. As a result, they showed that the limited layered Metafoundation is the most efficient solution for attenuating seismic waves.

Nonetheless, three basic issues remained unresolved: i) first, the optimization of multiple resonators acting in a linear LRM and associated with different parameters; second, the optimization of structural devices, i.e. springs and/or dampers, operating in the nonlinear regime within finite lattices; and third, the inclusion of the stochastic nature of seismic input.

With regard to the first, issue, i.e. the optimization of multiple resonators, the potential benefits of designing multiple resonators exhibiting both mass and bulk modulus dispersion between resonances are quite understood. More precisely, a metamaterial endowed with local resonators can exert an apparent negative mass as well as an apparent negative bulk modulus. These properties can be exploited for the attenuation of acoustic waves, and therefore, can be suitable adopted for the design of optimal multiple tuned resonators.

As far as the second issue is concerned, i.e. the selection of proper hysteretic dampers, Basone et al. [14] suggested to use wire ropes; they represent simple devices able to both effectively suspend concrete resonators inside the foundation and allow motion in all three main directions. Their behavior is quite complex and some researchers [16-18], among others, characterized their main nonlinear properties. More precisely, the mechanical flexibility of wire ropes provides good isolation properties and the sliding friction between the intertwined cables results in high dissipative capabilities. As a result, these devices can achieve equivalent damping ratios of 15-20 percent associated with low production and maintenance costs. Their hysteretic behavior can be reproduced with a well-known Bouc-Wen model [19,20]. This model is quite popular because can describes the behavior of a nonlinear hysteretic system with a compact first-order differential equation [21]. Due to its versatility and mathematical tractability, the Bouc-Wen model has gained popularity and has extensively been applied to a wide variety of seismic engineering problems. As a result, we have to deal with hysteretic systems, where nonlinearities depend on the history of the motion, rather than simply on the instantaneous motion.

In the same vein, the analysis of nonlinear metamaterials is still very challenging. For instance, from a perturbation approach specifically applied to weakly nonlinear periodic chains [8], emerges that: i) solutions to nonlinear wave equations are amplitude dependent; ii) wave amplitudes influence their own propagation characteristics, the so-called self-action; iii) analysis methods in the presence of self-action often do not trace all solutions when more than one dominant component is involved. Nonetheless, to both analyse and improve the performance of a metamaterial-based system several solutions are available. See among others, Yousefzadeh and Phani [22], which studied nonlinear transmission of wave energy in a finite dissipative periodic structure. They showed that there is a threshold for the driving amplitude above which a sudden

increase in the energy transmitted across the finite structure happens. This phenomenon for nonlinear finite lattices is due to a loss of stability of the periodic solutions that are initially localized to the driven end of the structure. The influence of damping, coupling strength and type of nonlinearity, i.e. hardening or softening are assessed. More precisely, they showed that: i) damping may eliminate the transmission phenomenon within a frequency range in the stop band; ii) an increase of strength of coupling between the units is found to increase the minimum force required for the onset of transmission; iii) the type of nonlinearity determines on which side of the pass band the enhanced transmission may occur. Zhou et alii [23] analyzed wave packet propagation in weakly nonlinear acoustic metamaterials and highlighted the interior nonlinear wave mechanism through a spectro-spatial analysis. They found that that type of analysis can provide detailed information about solitary waves in short wavelength regions which cannot be captured by the Lindstedt-Poincare' method. Moreover, they also found that optical wave modes in nonlinear metamaterial are sensitive to parameters of the nonlinear cubic constitutive relation. Zivieri et alii [24] started from the factorization of the spatial and temporal parts of the solution and a periodic distribution function as ansatz of a general solution of the temporal part of the nonlinear equations of motion (EoM). Hence, they derived an analytical nonlinear dispersion relation for nonlinear periodic mass-spring and mass-in-mass systems. A comparison with numerical simulations showed the range of validity of the proposed expressions. Moreover, Sheng et alii [25] systematically studied influences of amplitude, nonlinear stiffness coefficients, resonance frequencies, masses and beam thicknesses on the bandwidth and efficiency of vibration mitigation properties. Thus, in order to realize low-frequency, broadband and highly efficient vibration reduction with limited attached masses, they presented an optimized lightweight nonlinear acoustic metamaterial beam. Other studies dealing with nonlinear problems regard the so-called conceptual negative stiffness element (NSE) inserted in resonators of mass-in-mass periodic systems. More precisely, each NSE element can exerts a resulting force capable of assisting motion instead of opposing it: this effect can improve the whole system behaviour. A feasible mechanism for a finite lattice and the relevant effects on band gaps based on the harmonic balance linearization was proposed by Wenzel et al. [26].

As regards the third issue, i.e. the stochastic nature of the seismic input and the subsequent stochastic response analysis of hysteretic systems, a rich literature is available; see, among others, [12, 17, 26]. In this respect, the equivalent (stochastic) linearization technique (ELT) suggested by [27,28], based on a non-Gaussian probability density function is viable because can be extended, in a relatively straightforward manner to MDoF systems; pros and cons of this technique were discussed in [28].

1.2 Scope

In sum, in order to achieve the best performance of a finite LRM, the following objectives are pursued hereinafter: i) the optimal tuning of multiple resonators to different frequencies and damping via nonlinear programming within different configurations of metafoundations; ii) the optimization of the nonlinear behavior of wire ropes reproduced with hysteretic Bouc-Wen models and iii) to take into account the stochastic nature of seismic input both in the frequency and the time domain as well as the application of ELT to fully nonlinear devices.

The superstructure is represented by a fuel storage tank and its equivalent 2D lumped mass model [29]. Therefore, the objective function for both i) and ii) is represented by the relative drift or the absolute acceleration of the impulsive mode of the tank. In particular, the metafoundation is designed to remain undamaged for an active seismic site located in Priolo Gargallo, Sicily, Italy. The slender tank (superstructure) instead, was part of an existing plant. In view of a consistent seismic input for linear/nonlinear time history analyses, a set of natural earthquakes that correspond to safe shutdown earthquakes (SSE) events are selected from Italian and European databases and fitted in average to the uniform hazard spectrum (UHS) of Priolo Gargallo.

In order to take into account the stochastic nature of the seismic input, the computations are carried out in the frequency domain; and because the analysis of nonlinear periodic systems entails the aforementioned difficulties [8], an ELT is assumed for the Bouc-Wen model considered in objective ii). Therefore, an average power spectral density (PSD) function of those accelerograms is evaluated. The resulting PSD function is fitted with a Kanai-Tajimi filter [30] modified by Clough and Penzien [31] and, subsequently, adopted in the

optimization procedure. The resulting optimized Metafoundations were then verified through nonlinear time history analyses (THAs) of the coupled systems subjected to the aforementioned ground motions.
The rest of the paper is organized as follows. Firstly, details about the modelling of the various components of the coupled foundation-tank system are provided in Section 2. Section 3 provides the optimization procedure in the frequency domain when the foundation-tank system is composed of linear elements. The performance of the optimized system is verified by means of structural responses obtained with THAs for each considered case. Section 4 deals with the coupled system endowed with nonlinear components. In this case, the ELT is presented together with the optimization procedure. The choice of the optimal parameters of BW models that describe the hysteretic behavior of damper devices are discussed in Section 5, where the results of optimization are commented. Furthermore, each optimized nonlinear system is subject to verification by means of nonlinear THAs. Section 6 instead, presents both approximate and numerical spectral dispersion relationships for uncoupled periodic LRMs, together with topological (time-space domain) features of output waves traced by means of spectro-spatial analysis. Finally, conclusions and future developments are presented in Section 7.

2. Modelling of foundation-tank coupled system components

The finite LRM is composed by a finite number of unit cells realized with standard steel columns endowed with hollow sections and concrete slabs sketched in Fig. 1a. In each unit cell there are moving concrete masses, i.e. the resonators, that are linked via springs to the foundation as shown in Fig. 1b and Fig. 1c. The construction site was chosen to be Priolo Gargallo (Italy), which is characterized by a peak ground acceleration (PGA) of 0.56g at a return period of 2475 years. In agreement with the paper objectives stated in Subsection 1.2, the metafoundation was designed to remain undamaged even for safe shutdown events (SSE), according to the Italian seismic code [32].
Two foundations were designed with one and two layers of resonators, respectively. Both systems have a height of 4 m, and are comprised of columns, which represent the vertical load bearing system, and slabs that support the resonators. The columns are made of steel hollow sections and govern the horizontal stiffness of the structure. Their dimensions are 300x300 mm and 230x230 mm for the one and two layered case, respectively, while the wall thickness of the hollow section is 30 mm for both. These dimensions are the results of the linear elastic design according to the NTC 2018 [32] and determine the minimal allowable column stiffness.
The hydrodynamic response of liquid containers can be profitably simulated by means of the Housner's model [33]. The models can approximate internal actions for regular containers assuming that the water can be split into impulsive and convective masses. More recently, Malhotra [29] developed a simplified procedure for seismic analysis of cylindrical liquid-storage tanks. The relevant model reduces the tank response to the contribution of two main impulsive and convective modes, in which also the tank wall thickness is taken into account. Furthermore, in view of effectiveness, the concrete resonators are assumed to be suspended by wire ropes, as depicted in Fig. 1b and Fig. 1c, that allow each resonator motion in X, Y and Z directions. A sketch of a seismic record along X in Fig. 1c indicates the excitation direction. Details on the distribution of steel wire ropes in the single unit cell are provided in Fig. 2a.

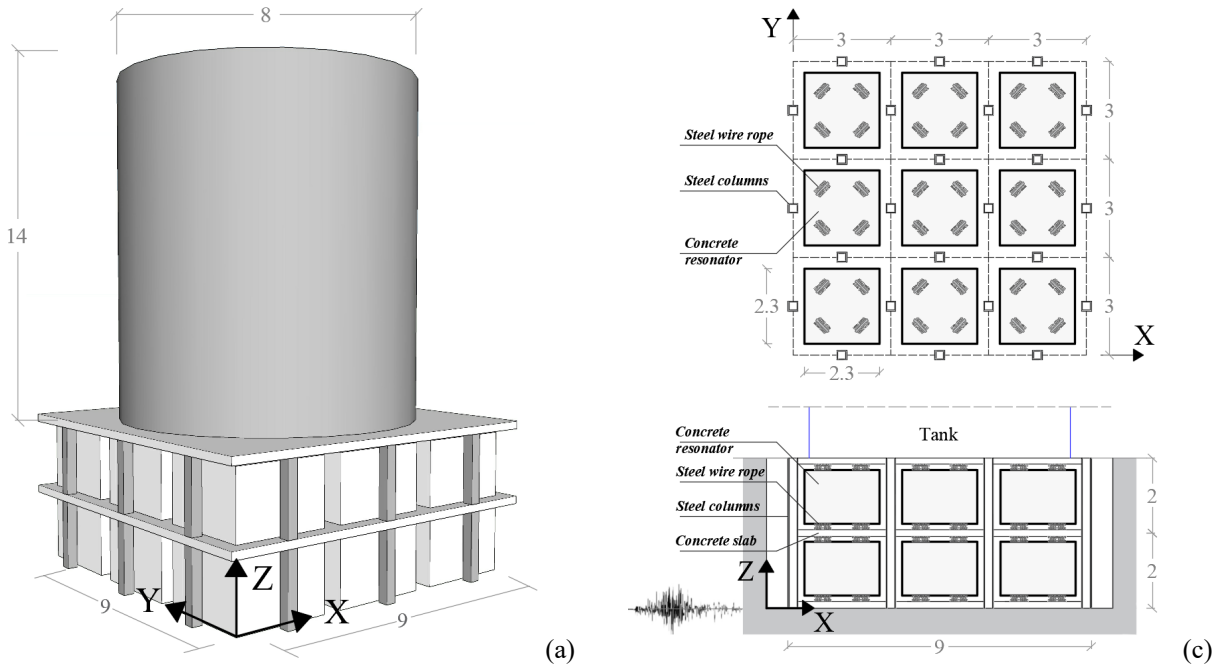

Fig. 1. Coupled foundation -tank system with two layers: (a) isometric view, (b) layout and (c) cross section and sketch of a seismic record along the X direction of excitation.

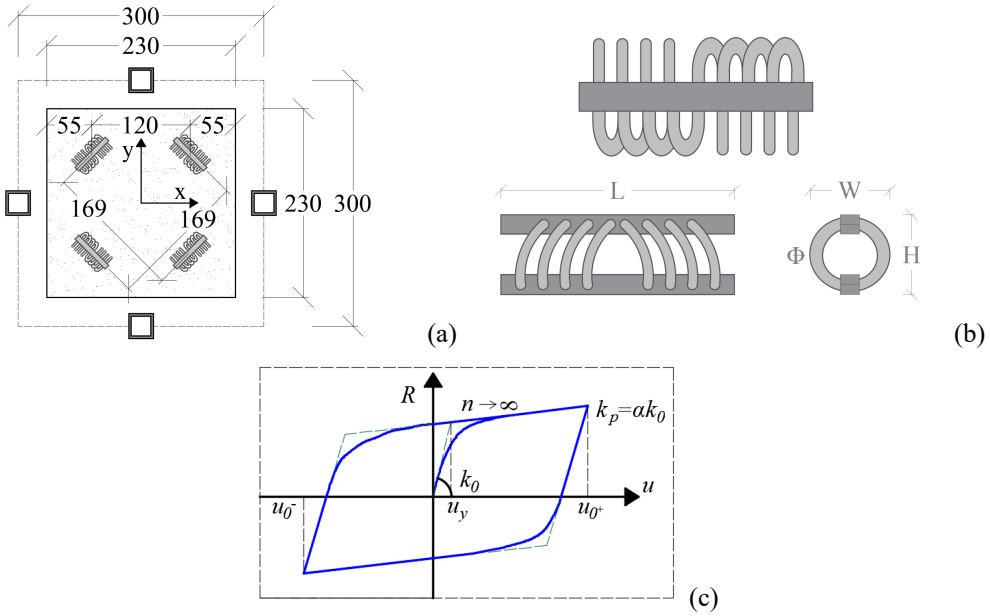

Fig. 2. (a) Configuration of a single unit cell equipped with steel wire ropes (measures in cm); (b) details of a single wire rope and (c) hysteretic loop of Bouc-Wen model.

2.1 Seismic metamaterial and negative apparent mass

In seismic engineering, two types of periodic materials are currently investigated: phononic crystals (PCs) and locally resonant acoustic metamaterials. The main advantage of both consists in designing a periodic structure that exhibits stop bands capable of forbidding elastic wave propagation within a desired frequency band. In particular, locally resonant acoustic metamaterials are more suitable than PCs at ultralow frequencies due to their capability to exhibit very low frequency band gaps, endowed with unit cells much smaller than the wavelength of the desired frequency region [2,4]. In this regard, the LRM depicted in Fig. 1 can be designed as a finite periodic system that allow to suppress seismic waves in certain frequency regions [14,15]; these regions, the so-called band gaps, are analytically defined through a lattice dispersion analysis using the Floquet–Bloch theorem. More precisely, it is possible to reduce the study of an infinite lattice to the analysis

of a single unit cell with Floquet-Bloch quasi-periodic boundary conditions. As a result, a frequency dispersion analysis can be carried out and the band gaps of the system can be found. More precisely, Fig. 3 shows the dispersion relation of an infinite periodic stack with linear properties, see, for instance, Fig. 14, of the unit cells described in Fig. 1. It demonstrates that a band gap forms in a predefined low-frequency range where elastic waves become evanescent.

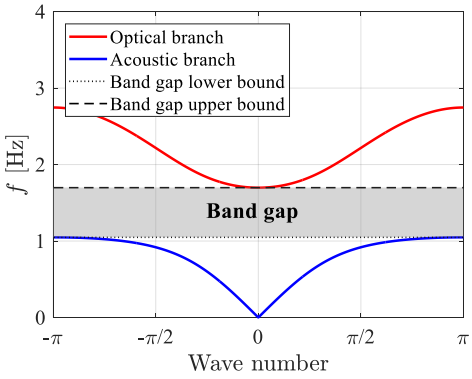

Fig. 3. Dispersion relation for an infinite stack of unit cells with the geometric properties of the two-layered foundation case (after [14])

It should be emphasized that these considerations are obtained considering the foundation system depicted in Fig. 1 as an infinite lattice. However, since the solution depicted in Fig. 1 is a finite metafoundation, further analyses are needed. In this regard, in order to decouple the mode of the foundation structure with that of the superstructure, well-known concepts of seismic isolation [34,35] drive the design of a foundation system versus large flexibility. It follows that the elastic design of the foundation required by NTC 2018 [32] provides minimum value of the columns cross-section depicted in Fig. 2a, to enhance flexibility.

Conversely, in order to achieve the largest antiresonance effects or the maximum attenuation effects, resonator masses are massive and compatible with cell geometry to exploit the negative apparent mass concept [2,4,5]. In this respect and based on Fig. 4, the apparent masses experienced by the exterior cells read,

$$M^1_{app}(\omega) = m_1 - \frac{k_1}{\omega^2} + \frac{k_2}{\omega_2^2 - \omega^2} \tag{1a}$$

$$M^2_{app}(\omega) = m_1 - \frac{k_1}{\omega^2} + \frac{k_2}{\omega_2^2 - \omega^2} + \frac{k_3}{\omega_3^2 - \omega^2} \tag{1b}$$

where m_1 and k_1 are the mass and stiffness of the exterior unit cell, m_2 and m_3 are masses, k_2 and k_3 are stiffnesses of resonators, ω_2 and ω_3 are relevant frequencies of resonators while ω represents the forcing frequency.

It is clear that the effective mass $M^1_{app}(\omega)$ becomes negative in Fig. 4a when the forcing frequency is close to resonance. Since the acceleration response is opposing to the applied force, the response amplitude is reduced and attenuation zones appear. This effect is greatly magnified as the input frequency ω approaches the local resonance frequency. Further enhancements can be obtained adding resonators with different resonant frequencies, as shown in Fig. 4b. Indeed, a double negativity can be observed close to the second resonant frequency of the system. As a result, further benefits can be obtained when multiple resonators are differently tuned [5]. These benefits will be achieved with different optimal configurations of Metafoundations presented in the next subsection.

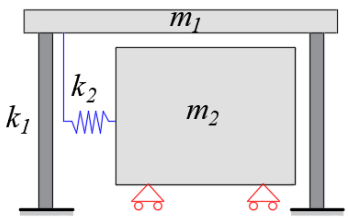

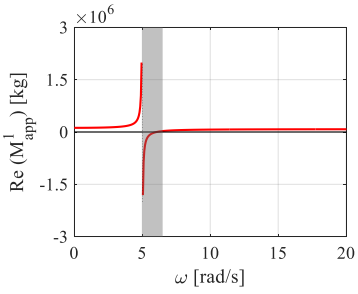

(a)

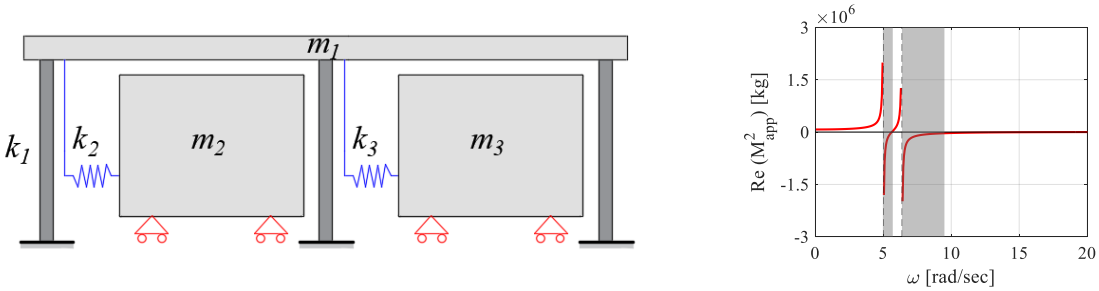

(b)

Fig. 4. Apparent mass as a function of forcing frequency: (a) single and (b) double unit mass-in-mass case.

2.2 System modelling and reduction

For simplicity and without loss of generality, we consider only a seismic input along the X direction. As a result, through dynamic condensation of both mass and stiffness, the foundation-tank coupled system sketched in Fig. 1 can be modelled as a full mass system (FMS) in the X-Z plane, as shown in Fig. 5a. The result of the dynamic condensation is exact since all resonators in the Y direction are assumed to be endowed with the same mass and stiffness in each layer.

In order to deal with simpler coupled systems and to take benefit in the optimization from different stiffness and damping values, both condensed mass (CMSs) and reduced mass systems (RMSs) have been also considered, as indicated in Fig. 5b and Fig. 5c, respectively. More precisely, to considerably reduce the computational effort during the optimization procedure, the CMS is obtained condensing all resonators in the X direction. However, CMS cannot benefit from different modal contributions in each layer. As a result, the RMS can consider different resonator parameters during the optimization, entailing a slight increase in computational effort. In the same veins, Fig. 5 shows the principal configuration of the three analyzed systems, for the two-layered case. Herein, m_i, c_i and k_i represent mass, stiffness and damping coefficients of the impulsive mass of the superstructure -tank-, respectively, while m_c, c_c and k_c represent mass, stiffness and damping coefficients of the relevant convective mass. We underline that resonators considered equal are endowed with the same mass and the same stiffness. This represents an ideal condition since statistically some variations of mass and stiffness exist. However, their variations are negligible in this study.

The system of equations of motions (EOMs) of the systems depicted in Fig. 5 reads,

$$\mathbf{M}\,\ddot{\mathbf{u}}(t) + \mathbf{C}\,\dot{\mathbf{u}}(t) + \mathbf{K}\,\mathbf{u}(t) = \mathbf{F}(t) \tag{2}$$

where $\mathbf{M}$, $\mathbf{C}$, and $\mathbf{K}$ are the mass, damping, and stiffness matrices, respectively, while $\ddot{\mathbf{u}}(t)$, $\dot{\mathbf{u}}(t)$ and $\mathbf{u}(t)$ denote acceleration, velocity, and displacement vectors. Furthermore, $\mathbf{F}(t) = -\mathbf{M}\boldsymbol{\tau}\,\ddot{u}_g(t)$ is the forcing vector, where $\boldsymbol{\tau}$ is the mass influence vector and $\ddot{u}_g(t)$ represents the ground acceleration.

In order to evaluate the dynamic properties of the RMS depicted in Fig. 5c, we employ the system equivalent reduction expansion procedure (SEREP) proposed by O'Callahan [36]. This procedure allows for the reduction of some modal vectors of the FMS systems. More precisely, the convective mode and the relevant DoF of the tank can be eliminated from the full set of 'n' DoFs, while the effects on the lower 'a' modes can be retained. Hence, the SEREP technique is based on the following transformation,

$$\mathbf{u}_n = \mathbf{T}\,\mathbf{u}_a \tag{3}$$

where $\mathbf{T} = \boldsymbol{\Phi}_n \boldsymbol{\Phi}_a^g$ is the transformation matrix, with $\boldsymbol{\Phi}_n$ being the modal matrix of the original system, while $\boldsymbol{\Phi}_a^g$ represents the generalized inverse of the modal matrix of the active/reduced system. More precisely, $\boldsymbol{\Phi}_a^g$ can be evaluated as,

$$\boldsymbol{\Phi}_a^g = \left(\boldsymbol{\Phi}_a^T \boldsymbol{\Phi}_a\right)^{-1} \boldsymbol{\Phi}_a^T \tag{4}$$

As a result, the system matrices of the reduced system read $\tilde{\mathbf{M}} = \mathbf{T}^T\mathbf{M}\,\mathbf{T}$, $\tilde{\mathbf{K}} = \mathbf{T}^T\mathbf{K}\,\mathbf{T}$ and $\tilde{\mathbf{C}} = \mathbf{T}^T\mathbf{C}\,\mathbf{T}$, while the forcing term becomes $\tilde{\mathbf{F}} = -\mathbf{T}^T\mathbf{M}\boldsymbol{\tau}\,\ddot{u}_g$. Since the optimization procedure requires an inversion of the transmission matrix $\mathbf{T}$ for each frequency interval, as illustrated in Section 3, SEREP also contributes to the reduction of the run time of optimization algorithms.

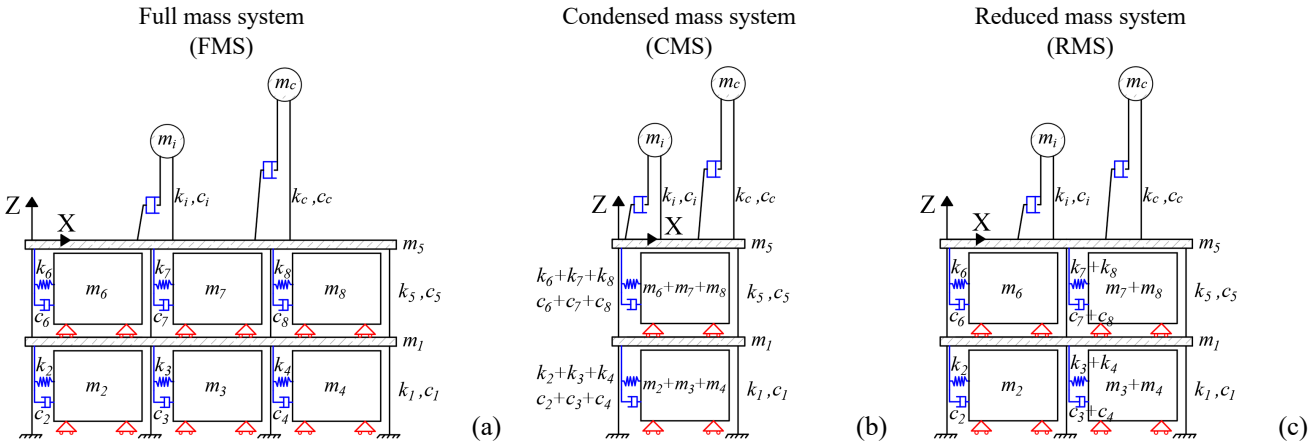

Fig. 5. Models of the Metafoundation for the two-layered case: (a) FMS; (b) CMS and (c) RMS.

2.3 Wire rope modelling

In order to model the nonlinear behavior of wire ropes, we employ the Bouc-Wen model, which has been extensively used in the literature to capture the hysteretic behavior of many seismic devices [19-21]. In accordance with this model, for a SDoF system we get

$$m\ddot{u}(t)+c\dot{u}(t)+R(t)=F(t) \tag{5}$$

where $R(t)$ defines the nonlinear restoring force,

$$R(t)=\alpha\, k\, u(t)+(1-\alpha)k\, u_y\, z(t) \tag{6}$$

In particular, k and u_y represent the yielding stiffness and displacement, respectively, whereas the dimensionless hysteretic component z is given by the solution of the nonlinear differential equation,

$$\dot{z}(t)=u_y^{-1}\left[A\dot{u}(t)-\gamma\left|\dot{u}(t)\right|\left|z(t)\right|^{n-1}z(t)-\beta\dot{u}(t)\left|z(t)\right|^{n}\right] \tag{7}$$

Here A, β, γ, and the exponent n are parameters that control the shape and smoothness of the force-displacement loop. Moreover in Eq. (6), $\alpha = k_p/k_0$ defines the post-yielding to pre-yielding stiffness ratio, with

$$k_0=\left(\frac{\partial R(u,\dot{u},z)}{\partial u}\right)_{z=0}=\alpha k+(1-\alpha)kA\,; \qquad k_p=\left(\frac{\partial R(u,\dot{u},z)}{\partial u}\right)_{z=z_{\max}}=\alpha k_0 \tag{8}$$

where $z_{\max}=\left[A/(\beta+\gamma)\right]^{1/n}$.

For suitable values of the parameters A, β, γ and n, the Bouc-Wen model can yield hardening or softening nonlinearities. A hardening behavior is simulated when $|\gamma|>|\beta|$ and $|\gamma|<0$; otherwise, a softening behavior is obtained. Furthermore, n modulates the sharpness of yield and when $n \to \infty$ the elasto-plastic hysteresis case is approached. By choosing n =1, Eq. (7) can be analytically solved with simple exponential functions [20,21]. Other parameter values used for the optimization process are discussed in Subsection 5.1.

2.4 Accelerogram selection and seismic input model

In order to evaluate the seismic activity of the construction site, i.e. Priolo Gargallo, a set of 12 natural accelerograms were selected from Italian and European database with 2% probability of exceedance in 50 years. These accelerograms are selected so that their mean spectrum fits in a least-square sense the uniform hazard spectrum (UHS) of Priolo Gargallo. It is well known that the UHS is often overly conservative because it combines the hazard from different sources and does not reflect a realistic spectrum that can be expected to occur during a single earthquake. However, the use of a conditional mean spectrum (CMS) that matches the UHS level only at the fundamental period of a system is overly complex and limiting for the problem to hand. Further details on the selection criteria of accelerograms are reported in Basone et al. [14].

The optimization procedures performed in the frequency domain, see Section 3 and 4, assume that the seismic input is a weakly stationary Gaussian filtered white noise random process with zero mean and spectral intensity S_0. In order to approximately take soil into account, we use the Kanai-Tajimi filter [30]; and to avoid unrealistic high values in the low-frequency range, a second filter in series proposed by Clough and Penzien [31] is adopted. For brevity, it is referred to as KTCP filter. The relevant power spectral density (PSD) function can be expressed as,

$$S_{\ddot{u}_g}(\omega) = S_0 \frac{4\zeta_g^2\omega_g^2\omega^2 + \omega_g^4}{4\zeta_g^2\omega_g^2\omega^2 + \left(\omega_g^2 - \omega^2\right)^2} \frac{\omega^4}{4\zeta_f^2\omega_f^2\omega^2 + \left(\omega_f^2 - \omega^2\right)^2} \tag{9}$$

where ω_g and ζ_g are the frequency and damping ratio that describe the soil characteristics, while ω_f and ζ_f denote the parameters of the low pass-filter [31], respectively.
In the time domain, the KTCP model is governed by the following differential equation,

$$\ddot{u}_g = \omega_g^2 u_g + 2\zeta_g\omega_g\dot{u}_g - \omega_f^2 u_f - 2\zeta_f\omega_f\dot{u}_f \tag{10}$$

which can be completed in a state-space variable form as follows,

$$\begin{aligned} \ddot{u}_g &= \mathbf{a}_f^{\,T}\,\mathbf{u}_f \\ \dot{\mathbf{u}}_f &= \mathbf{A}_f\,\mathbf{u}_f + \mathbf{V}_f\,f(t) \end{aligned} \tag{11a}$$

$$\mathbf{u}_f = \begin{bmatrix} u_f \\ \dot{u}_f \\ u_g \\ \dot{u}_g \end{bmatrix}; \quad \mathbf{a}_f = \begin{bmatrix} -\omega_f^2 \\ -2\zeta_f\omega_f \\ \omega_g^2 \\ -2\zeta_g\omega_g \end{bmatrix}; \quad \mathbf{A}_f = \begin{bmatrix} 0 & 1 & 0 & 0 \\ -\omega_f^2 & -2\zeta_f\omega_f & \omega_g^2 & 2\zeta_g\omega_g \\ 0 & 0 & 0 & 1 \\ 0 & 0 & -\omega_g^2 & -2\zeta_g\omega_g \end{bmatrix}; \quad \mathbf{V}_f = \begin{bmatrix} 0 \\ 0 \\ 0 \\ 1 \end{bmatrix} \tag{11b}$$

where $f(t)$ is the bedrock Gaussian zero-mean white-noise process. The filter parameters are chosen to match the ground motion characteristics of Priolo Gargallo, at a return period of 2475 years. More precisely, the parameters of KTCP filter fit in a least square sense the stationary PSD function of the aforementioned 12 accelerograms [14]. Their values amount to $S_0 = 0.09$ (m^2/s^3), $\omega_g = 14$ (rad/s), $\zeta_g = 0.6$, $\omega_f = 0.75$ (rad/s) and $\zeta_f = 1.9$.

3. Optimization of a Metafoundation endowed with linear devices

The proposed Metafoundation is characterized by two sets of parameters: (i) parameters that derive from construction or feasibility constraints, e.g. column size, slab thickness, etc.; and (ii) parameters that can be chosen more freely, i.e. stiffness and damping parameters of the resonators. In this regard, to maximize antiresonance or negativity effects, see Subsection 2.1, masses of resonators are set as the largest mass compatible with the unit cell dimensions. This consideration is consistent with both metamaterials and tuned mass dampers discussed in [3-6, 14].
Owing to the seismic input defined in Eq. (9), the herein proposed optimization procedure is based on computations in the frequency domain, and can, in principle, optimize any number of parameters. The application of the Fourier transform to Eq. (2), entails,

$$-\omega^2\mathbf{M}\,\mathbf{u}(\omega) + i\omega\,\mathbf{C}\,\mathbf{u}(\omega) + \mathbf{K}\,\mathbf{u}(\omega) = \mathbf{F}(\omega) \tag{12}$$

where ω represents the circular frequency. From Eq. (12) we can define the transmission matrix $\mathbf{H}(\omega)$ as follows,

$$\mathbf{H}(\omega) = \left[-\omega^2\mathbf{M} + i\omega\,\mathbf{C} + \mathbf{K}\right]^{-1} \tag{13}$$

Therefore, the PSD of the j-th DoF can be approximated with[29],

$$S_{Q_j}(\omega) = \left|H_j(\omega)\right|^2 S_{\ddot{u}_g}(\omega) \tag{14}$$

where $H_j(\omega)$ and $S_{\ddot{u}_g}(\omega)$ are the j-th transfer function component and the PSD of the force acting on the system, respectively. Therefore, we assume be valid for a weakly stationary random process, the Wiener–

Khinchin theorem such that R(τ) and the PSD are a Fourier-transform pair. As a result, the autocorrelation function R(τ) and the PSD satisfy the necessary conditions for Fourier inversion,

$$\sigma_j^2 = \int_0^{+\infty} \mathrm{S}_{Q_j}(\omega)\, d\omega \tag{15}$$

where $\sigma_j^2 = \mathrm{R}(\tau=0)$ is the variance of the response of the j-th DoF of the system. The optimization criterion is chosen to be the minimization of the interstory drift or the absolute acceleration of the impulsive mode of the tank. Note, that for slender tanks, this mode has proven to dominate the base shear response of the whole system. Moreover, from Eq. (5), for the linear case, one obtains,

$$\left| m\, \ddot{u}_{tot} \right| = \left| -c\, \dot{u} - k\, u \right| \tag{16}$$

where the relationship between interstory drift and absolute acceleration depend on damping forces. Therefore, the variance of the interstory drift and the absolute acceleration read,

$$\sigma_{dr_{imp}}^2 = \int_0^{+\infty} \left| \mathrm{H}_{imp}(\omega) - \mathrm{H}_{tl}(\omega) \right|^2 S_{\ddot{u}_g}(\omega)\, d\omega \tag{17a}$$

$$\sigma_{acc_{imp}}^2 = \int_0^{+\infty} \left| 1 - \omega^2 \mathrm{H}_{imp}(\omega) \right|^2 S_{\ddot{u}_g}(\omega)\, d\omega \tag{17b}$$

where $\mathrm{H}_{imp}(\omega)$ and $\mathrm{H}_{tl}(\omega)$ are the transfer functions of the impulsive mass and top layer, respectively. Furthermore, the dimensionless performance indices can be defined as follows,

$$\mathrm{PI}_{dr} = \frac{\sigma_{dr_{imp}}^2}{\sigma_{dr_{imp}}^{2\ fix}} \tag{18a}$$

$$\mathrm{PI}_{acc} = \frac{\sigma_{acc_{imp}}^2}{\sigma_{acc_{imp}}^{2\ fix}} \tag{18b}$$

where $\sigma_{dr_{imp}}^{2\ fix}$ and $\sigma_{acc_{imp}}^{2\ fix}$ represent the variances of interstory drift and absolute acceleration impulsive mass, respectively, based on a tank without foundation, i.e. a fixed-base tank. These indices provide an estimation of the response reduction, and therefore, need to take up their minimal value for an optimal coupled system.

3.1 Optimization problem

The design variables $\xi_{k,n}$ and $f_{k,n}$ define damping ratio and frequency of the *n*-th resonator in the *k*-th layer, respectively. They are collected in the parameter vector,

$$\mathbf{X} = \left[\zeta_{1,1}, \zeta_{k,n}, f_{1,1}, f_{k,n} \right]^{\mathrm{T}} \tag{19}$$

Therefore, the optimization problem can thus be stated,

$$\min_{k,n}\ \mathrm{PI}_{dr}(\mathbf{X}) \ \text{ or } \ \min_{k,n}\ \mathrm{PI}_{acc}(\mathbf{X}) \tag{20}$$

for CMS, RMS and FMS cases, respectively Furthermore, the following bounds hold,

$$0.05 \le \zeta_{k,n} \le 0.20 \ \text{ and } \ 1\mathrm{Hz} \le f_{k,n} \le 4\mathrm{Hz} \tag{21}$$

Details on the chosen bounds in Eq. (21) are provided in Subsection 3.2.

The optimization procedure is carried out with the aid of a numerical search algorithm, i.e. the built-in MATLAB `fmincon` function. It implements a nonlinear programming solver, based on the interior-point algorithm, with embedded constraint functions for the sought tuning variables collected in the parameter vector **X**.

3.2 Optimization results

The optimization procedure described in Subsection 3.1 is carried out for all CMS, RMS and FMS, for both one and two-layered foundation cases. In this respect, Table 1 summarizes the values for CMS, while Tables Table 2 and Table 3 show the results for RMS, and FMS, respectively.

Table 1
Optimal parameters of the CMS for both one and two-layered cases.

One-layered case (k=1)			
Performance index		$f_{1,1}^{opt}$ [Hz]	$\zeta_{1,1}^{opt}$
PI_{dr}	0.677	2.5	0.20
PI_{acc}	0.845	2.5	0.20

Two-layered case (k=1,2)					
Performance index		$f_{1,1}^{opt}$ [Hz]	$\zeta_{1,1}^{opt}$	$f_{2,1}^{opt}$ [Hz]	$\zeta_{2,1}^{opt}$
PI_{dr}	0.807	2.6	0.10	3.6	0.18
PI_{acc}	0.877	2.6	0.10	3.6	0.18

Table 2
Optimal parameters of the RMS for both one and two-layered cases.

One-layered case (k=1)							
Performance index		$f_{1,1}^{opt}$ [Hz]	$\zeta_{1,1}^{opt}$	$f_{1,2}^{opt}$ [Hz]	$\zeta_{1,2}^{opt}$	$f_{1,3}^{opt}$ [Hz]	$\zeta_{1,3}^{opt}$
PI_{dr}	0.618	3.4	0.16	2.2	0.17	2.2	0.17
PI_{acc}	0.783	3.4	0.16	2.2	0.17	2.2	0.17

Two-layered case (k=1,2)													
Performance index		$f_{1,1}^{opt}$ [Hz]	$\zeta_{1,1}^{opt}$	$f_{1,2}^{opt}$ [Hz]	$\zeta_{1,2}^{opt}$	$f_{1,3}^{opt}$ [Hz]	$\zeta_{1,3}^{opt}$	$f_{2,1}^{opt}$ [Hz]	$\zeta_{2,1}^{opt}$	$f_{2,2}^{opt}$ [Hz]	$\zeta_{2,2}^{opt}$	$f_{2,3}^{opt}$ [Hz]	$\zeta_{2,3}^{opt}$
PI_{dr}	0.802	2.6	0.15	2.6	0.15	2.6	0.15	3.0	0.15	3.8	0.16	3.8	0.16
PI_{acc}	0.873	2.6	0.15	2.6	0.15	2.6	0.15	3.0	0.15	3.8	0.16	3.8	0.16

Table 3
Optimal parameters of the FMS for both one and two-layered cases.

One-layered case (k=1)							
Performance index		$f_{1,1}^{opt}$ [Hz]	$\zeta_{1,1}^{opt}$	$f_{1,2}^{opt}$ [Hz]	$\zeta_{1,2}^{opt}$	$f_{1,3}^{opt}$ [Hz]	$\zeta_{1,3}^{opt}$
PI_{dr}	0.617	2.2	0.15	3.4	0.16	2.2	0.18
PI_{acc}	0.776	2.0	0.12	3.4	0.16	2.4	0.14

Two-layered case (k=1,2)													
Performance index		$f_{1,1}^{opt}$ [Hz]	$\zeta_{1,1}^{opt}$	$f_{1,2}^{opt}$ [Hz]	$\zeta_{1,2}^{opt}$	$f_{1,3}^{opt}$ [Hz]	$\zeta_{1,3}^{opt}$	$f_{2,1}^{opt}$ [Hz]	$\zeta_{2,1}^{opt}$	$f_{2,2}^{opt}$ [Hz]	$\zeta_{2,2}^{opt}$	$f_{2,3}^{opt}$ [Hz]	$\zeta_{2,3}^{opt}$
PI_{dr}	0.802	3.6	0.16	3.6	0.18	2.6	0.16	3.6	0.16	3.6	0.18	2.6	0.16
PI_{acc}	0.870	3.6	0.20	2.6	0.20	3.4	0.16	3.6	0.20	2.6	0.20	3.4	0.16

When comparing the different systems to each other, the PI value slightly decreases from CMS to RMS. The RMS allows for the increase of the performance of the system due to resonant phenomena between two resonators tuned to different frequencies. Conversely, no significant advantage is obtained with the FMS due to fact that a further optimized resonator does not allow for the activation of significant resonance phenomena. This consideration is consistent with concepts of double negativity described in Subsection 2.1. However, these reductions are very small mainly due to the fact that we adopt resonator maximum masses, compatibly to unit cell dimensions. In sum, the mass of the resonators provides a great contribution in the seismic isolation of the system [14]; therefore, resonators tuning with different frequencies and damping ratios does not provide a significant contribution on the performance of the Metafoundation.

The optimization of the PI via the interstory drift or the absolute acceleration of the superstructure yield almost the same values for resonator frequencies and damping. In fact, interstory drift and absolute acceleration of the impulsive mode of the tank differ only through damping forces as implied by Eq. (16). Damping ratios, on the other hand, seem to decrease when multiple resonators are tuned to different frequencies. This could potentially be useful when it may be difficult to achieve high damping ratios.

With regard to the bounds of Eq. (21), Fig. 6a shows the optimization plane of the one-layered CMS with its corresponding contour lines. This surface is obtained removing the upper bound of $\zeta_{k,n}$ in order to show the trend of the optimization surface as a function of the damping ratio. It is evident that when the damping ratio exceeds a certain threshold, the advantage gained on PI_{dr} is minimal. Moreover, Fig. 6b depicts the

optimization plane of the one-layered RMS case, where the x and y-axis denote the frequencies of the two independent resonators. The contour lines of this plot show a wide area for the optimal values of the two resonators, where the value of the PI does not change significantly. Clearly, the resonators can be tuned to any set of two frequencies in this area, without inhibiting the functionality of the metafoundation. Similar to the aforementioned damping ratio trend, this could have positive effects for practical applications, where the tuning of the resonators may not be very precise. In sum, the optimization of multiple resonators with different frequencies and damping ratios offer a slight advantage in terms of demand reduction from CMS to RMS, while no advantages are obtained with FMS. However, a system with optimal multiple resonators may be employed due to technological constraints.

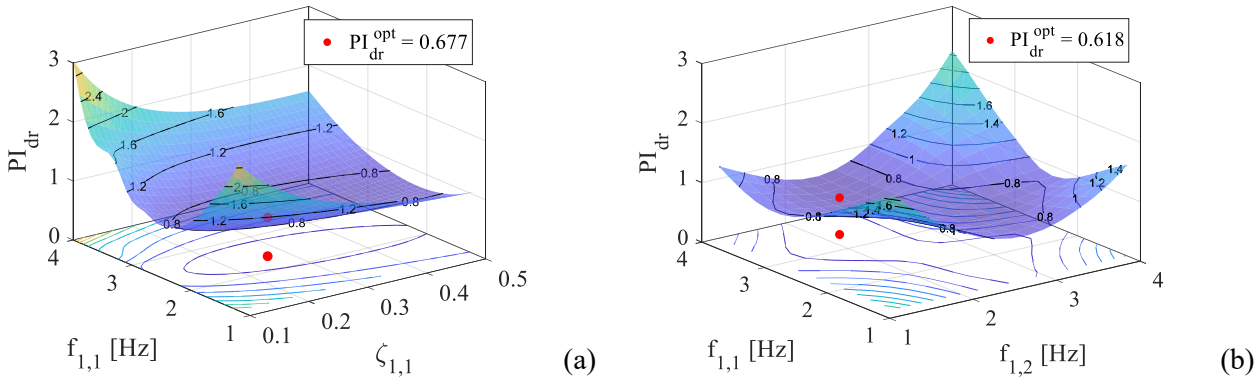

Fig. 6. Optimization surfaces of one-layered (a) CMS case and (b) RMS case.

3.3 Time history analyses results

In order to verify the results of the previous Subsection and to take into account the actual amplitude and phase variation of seismic waves, the performance of the optimized Metafoundation is evaluated with time history analyses (THSs). Therefore, the Metafoundation is subjected to the 12 natural seismic waves corresponding to a safe shutdown event (SSE) in the Priolo Gargallo site [14]. As a reference indicator, we use the root-mean square of the tank base shear V_{rms},

$$V_{rms} = \sqrt{\frac{1}{n}\sum_{j}^{n}\left(k_i\left(u_j^{imp} - u_j^{tl}\right) + k_c\left(u_j^{conv} - u_j^{tl}\right)\right)}, j = 1, \ldots, n \tag{22}$$

where, u_j^{imp}, u_j^{conv} and u_j^{tl} denote the displacement of the impulsive mass, the convective mass, and the top layer of the foundation, respectively, while n defines the number of time steps. The same quantities a_{rms} and d_{rms} have been evaluated for both absolute acceleration and interstory drift of the impulsive mass.

Fig. 7 shows the aforementioned quantities as a function of PGA. More precisely, they compare the results of THAs obtained for the optimized one-layered CMS on both PI_{dr} and PI_{acc} with the results of the fixed-base tank. It is worth noting that the results of the THAs show a high dispersion for *rms* values. Therefore, PGA may not represent the most significant intensity measure for the engineering demand parameters under consideration. Nonetheless, since we are not interested in a fragility analysis of the system, the PGA has been considered as a sufficient parameter for result interpretation [14,34].

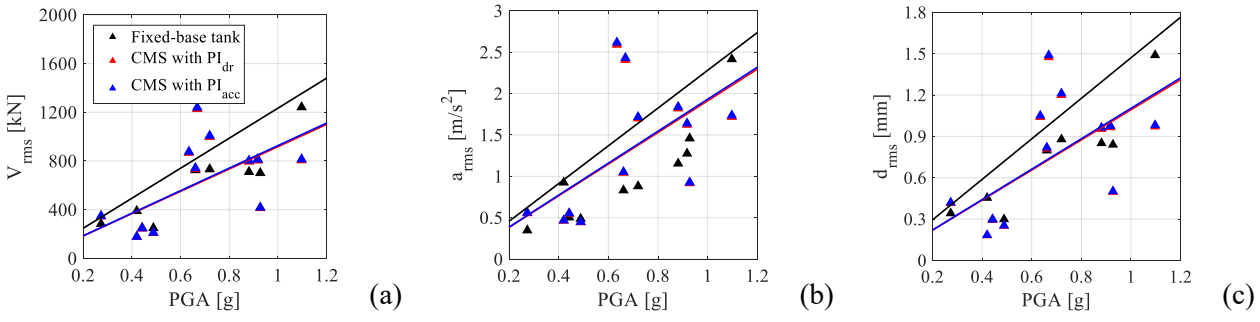

Fig. 7. Root mean square values of the (a) base shear, (b) interstory drift and (c) absolute acceleration of one-layered CMS for both PI_{dr} and PI_{acc}.

Nonetheless in the average, V_{rms} values are below values corresponding to the fixed-based tank. Moreover, similar results can be obtained with a_{rms} and d_{rms} for both PI_{dr} and PI_{acc}. Therefore, the following results will be expressed in terms of V_{rms} only.

Along the same lines, both Fig. 8a and Fig. 8b depict Vrms values for the one and two layered RMSs, respectively; similarly, Fig. 8c and Fig. 8d show results for the FMS case. It becomes apparent that all systems perform on a comparable level, independently of the number of individual resonators in the system or the chosen optimization parameter. The only major difference that can be noticed is that the systems with only one layer outperforms the systems with two layers. This is due to the fact that the one-layered foundations offer the same total height of 4 m, and therefore, exhibit a significantly lower horizontal stiffness of the outer cells. This trend is consistent with the finding of Basone at al. [14].

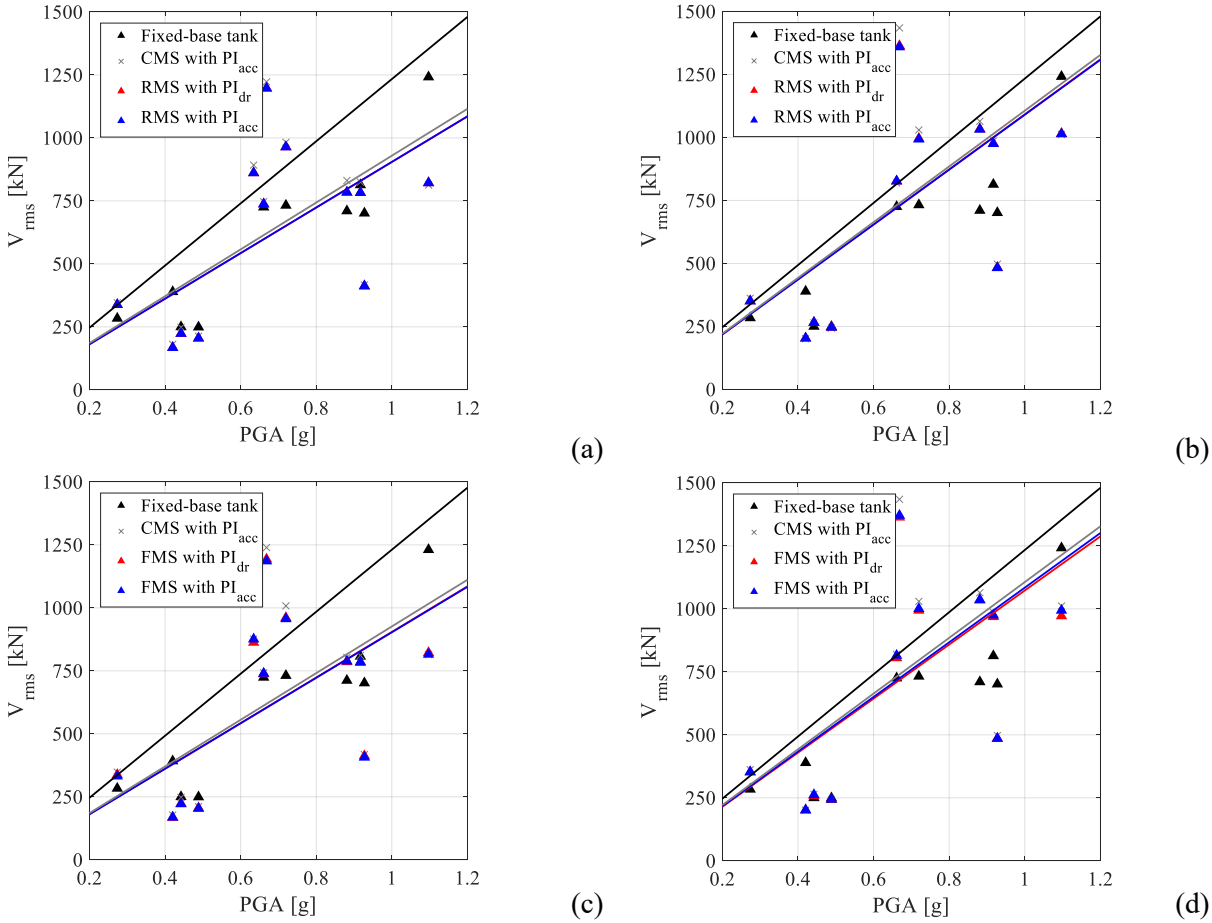

Fig. 8. Root mean square values of the tanks base shear for: (a) one-layered RMS; (b) two-layered RMS; (c) one-layered FMS; (d) and two-layered FMS

4. Optimization of a Metafoundation endowed with fully nonlinear devices

Motivated by the use of simple hysteretic devices, i.e. the wire ropes [16, 17, 14] able to both effectively suspend concrete resonators inside the LRM, allow motion in all three main directions and provide significant damping, herein we propose an optimization procedure based on the stochastic linearization technique [27,28]. In addition, the treatment of a linearized system allows to bypass several difficulties related to the definition of dispersion properties of a nonlinear periodic system as discussed in Section 6.

Similar to the linear case, we need to define a set of parameters to be optimized. These parameters, are chosen among the parameters of the Bouc-Wen model introduced in Subsection 2.3. In the same veins, we start with the following system of EOMs,

$$\mathbf{M}\,\ddot{\mathbf{u}}(t) + \mathbf{C}\,\dot{\mathbf{u}}(t) + \mathbf{K}\,\mathbf{u}(t) + u_y\,\mathbf{K}^{NL}\mathbf{z}(t) = \mathbf{F}(t) \tag{23}$$

where $\mathbf{K}^{\mathrm{NL}}$ defines the nonlinear component of the stiffness matrix that contains the terms $(1 - \alpha_n)\, k_n$ introduced in Eq. (6). In this model, n denotes the n-th resonator of the system, while $\mathbf{z}(t)$ is the vector that contains the components $z_n(t)$ of the n-th resonator. Since Eq. (23) defines a nonlinear system, it is not amenable to the classical linear random vibration theory introduced in Section 3. Therefore, a stochastic linearization technique (ELT) is employed to replace the nonlinear vector $\mathrm{u}_y\, \mathbf{K}^{\mathrm{NL}} \mathbf{z}(t)$.

4.1 Equivalent linearization technique

The ELT is a relatively straightforward tool to define an equivalent linear system, equating its stochastic response to the response of a nonlinear system. More precisely, for a SDoF system with $N = 1$, the nonlinear differential equation Eq. (7) becomes,

$$\dot{z} + c_{eq}\dot{u} + k_{eq} z = 0 \tag{24}$$

where c_{eq} and k_{eq} are linearization coefficients that are "equivalent" in a statistical sense [27,28, 37, 38]. At this stage, it is useful to introduce a state-space formulation of Eq. (23) and Eq. (24),

$$\frac{d}{dt}\mathbf{Y} = \mathbf{G}\,\mathbf{Y} + \mathbf{V}\, f(t) \tag{25}$$

with,

$$\mathbf{Y} = \begin{bmatrix} \mathbf{u} \\ \dot{\mathbf{u}} \\ \mathbf{z} \\ \mathbf{u}_f \end{bmatrix}; \quad \mathbf{G} = \begin{bmatrix} \mathbf{0}_{N\mathrm{x}N} & \mathbf{I}_{N\mathrm{x}N} & \mathbf{0}_{N\mathrm{x}N} & \mathbf{0}_{N\mathrm{x}r} \\ -\mathbf{M}^{-1}\mathbf{K}^{L} & -\mathbf{M}^{-1}\mathbf{C} & -\mathbf{M}^{-1}\mathbf{K}^{NL} & -\mathbf{1}\,\mathbf{a}_f^{\,T} \\ \mathbf{0}_{N\mathrm{x}N} & -\mathbf{c}_{eq} & -\mathbf{k}_{eq} & \mathbf{0}_{N\mathrm{x}r} \\ \mathbf{0}_{r\mathrm{x}N} & \mathbf{0}_{r\mathrm{x}N} & \mathbf{0}_{r\mathrm{x}N} & \mathbf{A}_f \end{bmatrix}; \quad \mathbf{V} = \begin{bmatrix} \mathbf{0}_{N\mathrm{x}1} \\ \mathbf{0}_{N\mathrm{x}1} \\ \mathbf{0}_{N\mathrm{x}1} \\ \mathbf{V}_f \end{bmatrix} \tag{26}$$

where $\mathbf{Y}$ is the state-space vector, $\mathbf{K}^{L}$ and $\mathbf{K}^{NL}$ define the linear and nonlinear components of the stiffness matrix, respectively, while $\boldsymbol{k}_{eq}$ and $\boldsymbol{c}_{eq}$ represent the matrices including the equivalent linear coefficients. Moreover, N defines the number of DoFs of the system and $r = 4$ defines the number of equations of the KTCP filter introduced in Subsection 2.4.

Let the covariance matrix of $\mathbf{Y}$ be $\mathbf{S}$ with $S_{ij} = E[y_i\, y_j]$. Then, we assume that the seismic input is stationary. The solution of Eq. (25) can be derived from the following Lyapunov system of equations,

$$\mathbf{G}\,\mathbf{S} + \mathbf{S}\,\mathbf{G}^{T} + \mathbf{B} = \mathbf{0} \tag{27}$$

where $\mathbf{B}$ is a zero matrix except for the generic diagonal element corresponding to the nonzero row of the forcing function vector, i.e. $B_{ij} = 2\pi S_0$. Eq. (27) was solved with the algorithm proposed by Bartels and Steward [39]. Because $\boldsymbol{k}_{eq}$ and $\boldsymbol{c}_{eq}$ are not known a priori, an iterative solution procedure is required. In this regard, Maldonado et al. [37] suggested to set as initial values $c_{eq} = 1$ and $k_{eq} = 0.05\,(\beta + \gamma)$ for a faster convergence. Further details about the whole procedure based on a third order statistical linearization are available in [37,38] whilst a more elaborated variant of ELT based on Spanos and Giaralis [42] is discussed in Section 6.

4.2 Linearized devices optimization

In order to define the transfer function $\mathbf{H}(\omega)$ of the coupled systems depicted in Fig. 5 we start from Eq. (5). In fact, Eq. (25) includes the KTCP filter and the derivation is more burdensome. Therefore, the relevant $\mathrm{H}(\omega)$ for a SDoF reads,

$$\mathrm{H}(\omega) = \left[-\omega^2 m + i\omega c + \alpha k - \frac{i\omega}{i\omega + k_{eq}} c_{eq}\,(1-\alpha)\, k u_y \right]^{-1} \tag{28}$$

where the derivation details can be found in Appendix A. Its generalization reads,

$$\mathbf{H}(\omega) = \left[-\omega^2 \mathbf{M} + i\omega\, \mathbf{C} + \mathbf{K} + \mathbf{K}^{\mathrm{eq}} \right]^{-1} \tag{29}$$

where $\mathbf{K}^{\mathrm{eq}}$ cointains terms zero terms except those in which the n-th resonator is physically connected to the k-th layer of the Metafoundation as depicted in Fig. 5. More precisely, the nonzero terms k_{ij}^{eq} of matrix $\mathbf{K}^{\mathrm{eq}}$ read,

$$k_{ij}^{eq} = -\frac{i\omega}{i\omega + k_{eq}} c_{eq} (1-\alpha_n) u_y k_n \tag{30}$$

in which α_n and k_n are referred to the n-th resonator of the Metafoundation. Note the Eq. (29) degenerates into Eq. (13) when α = 1.

4.3 Optimization problem

The optimization procedure for the nonlinear devices relies on the design variables $k_{k,n}$ and $\beta_{k,n}$ gathered in the parameter vector $\mathbf{X}^{\mathrm{NL}}$,

$$\mathbf{X}^{\mathrm{NL}} = \left[k_{1,1}, k_{k,n}, A_{1,1}, A_{k,n}, \beta_{1,1}, \beta_{k,n}, \gamma_{1,1}, \gamma_{k,n} \right]^{\mathrm{T}} \tag{31}$$

Therefore, the optimization problem can be stated as,

$$\min_{k,n} \ \mathrm{PI}_{dr}\left(\mathbf{X}^{\mathrm{NL}}\right) \ \text{or} \ \min_{k,n} \ \mathrm{PI}_{acc}\left(\mathbf{X}^{\mathrm{NL}}\right) \tag{32}$$

where k=1,…,n_k and n=1,…,n_r. Finally, bounds on the design variable $\beta_{k,n}$ are,

$$0 < \beta_{k,n} < 1 \tag{33}$$

Further details about the bound in Eq. (33) are provided in Subsection 5.1.

5 Hysteretic dampers, Bouc-Wen parameters and optimization results

5.1 Hysteretic dampers and Bouc-Wen parameters

The optimization procedure presented in Section 4 allows for the evaluation of main parameters of a Bouc-Wen model employed to reproduce a hysteretic damper. With regard to hysteretic devices, steel wire ropes schematically depicted in Fig. 2b, represent a commonly used solution in seismic engineering due to their capability to dissipate a relatively large amount of energy. Moreover, they are fairly cheap both in terms of production and maintenance costs. Furthermore, they allow for an effective motion of the resonators along X, Y and Z as indicated in Fig. 1. Many authors investigated the effectiveness of wire ropes subjected to shear forces; see, among others, [16-18]. In this respect, Paolacci and Giannini [16] fitted the parameters of a Bouc-Wen model to sets of experimental data. As a result, we selected the wire rope WR36-400-08; its geometric dimensions are collected in Table 4 and the relevant nomenclature can be found in Fig. 9b. In particular, k_p and R_v represent the horizontal stiffness and the vertical load-bearing capacity, respectively. The authors have found $\alpha = 0.254$ and $u_y = 2.2$ mm; in addition, the quality of the fitting can be appreciated in Fig. 9a.

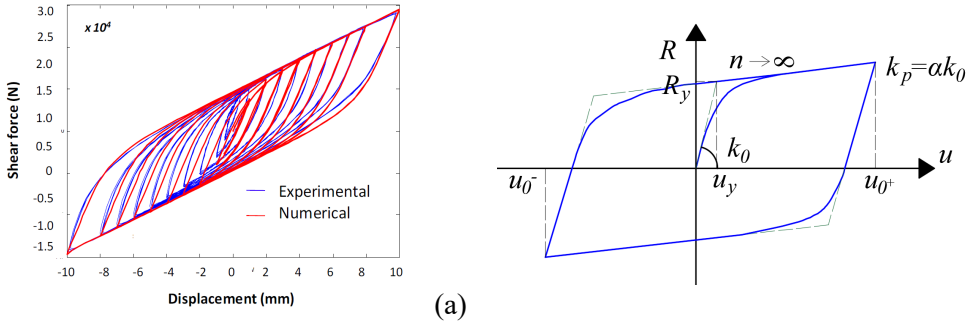

(a) (b)

Fig. 9. (a) Hysteretic behavior under cyclic shear loading (after Paolacci and Giannini [**Error! Reference source not found.**]) and (b) typical hysteretic loop of a Bouc-Wen model.

Table 4
Geometric and mechanical properties of wire ropes.

Geometric characteristics				Parameters of Bouc-Wen model					
H [mm]	W [mm]	L [mm]	Φ [mm]	k_0 [kN/mm]	R_y [kN]	u_y [mm]	n	A	α
178	216	520.7	26.6	1.35	2.97	2.2	1.0	1.0	0.254

The aforementioned wire ropes have also been successfully used in finite LRMs for the protection of slender storage tanks against vertical ground accelerations [40]. More precisely, two different configurations have been used: i) the same layout of Fig. 1, the so-called aligned column solution; ii) a configuration with columns at the second level staggered with respect to those at the first level, the so-called staggered column solution; thus, the additional slabs flexural stiffness was taken into account.

Once established the geometric and mechanical characteristics of a typical wire rope, some considerations on Bouc-Wen parameters need to be made. In fact, some parameters of the Bouc-Wen model presented in Subsection 2.3 are functionally redundant and can be appropriately set. More precisely, Charalampakis and Koumousis [20] reported that by setting A=1 and $\beta + \gamma = 1$, the model collapses to a rate-dependent Maxwell model with a nonlinear dashpot, i.e. an Ozdemir model. As a result, with A=1 in Eq. (8), the value of the initial stiffness $k = R_y / u_y = k_0$ is retrieved. Furthermore, $z_{max} = \left[A / (\beta + \gamma) \right]^{1/n} = 1$ and $z \in [-1, 1]$ in Eq. (7). Finally, thermodynamic admissibility issues [41] would require the inequality $\beta \leq \gamma$ to be satisfied; for the sake of generality, the aforementioned inequality is not strictly satisfied herein: thus, both bulge and slim-S shapes of the Bouc-Wen model are allowed.

5.2 Optimization results and time history analyses

The results of Subsection 3.3 underscore that only small differences in base shear values of the superstructures are achieved with CMS, RMS and FMS in the linear case; therefore herein, only optimizations of one and two-layered of CMS are carried out. In Subsections 5.1 we set n, α and u_y based on the properties collected in Table 4. As a result, we search for optimal values of k, β and γ with the constraints A=1 and $\beta + \gamma = 1$, respectively.

The results of optimization based on PI_{dr} are depicted in both Fig. 10a and Fig. 10b, for one-layered CMS and two-layered CMS, respectively. Notably, k2 represents the horizontal stiffness of a single resonator of the Metafoundation. Fig. 10a highlights a smooth surface in the range 50-60 kN/mm for the one-layered case; conversely, a narrow valley of possible optimal stiffness values characterizes the two-layered case. Furthermore, the two-layered CMS shows poor results in terms of PI_{dr} due to the increased horizontal stiffness of the system. The parameters β and γ quantify the dissipation characteristics of wire ropes; one can observe that an increase of β, i.e. a decrease of γ, does not entail a significant reduction of PI_{dr}. In fact, the constraint $\beta + \gamma = 1$ strongly sets the shape of the backbone loops and the relevant dissipated energy, as shown by the loops -in blue- depicted in Fig. 11.

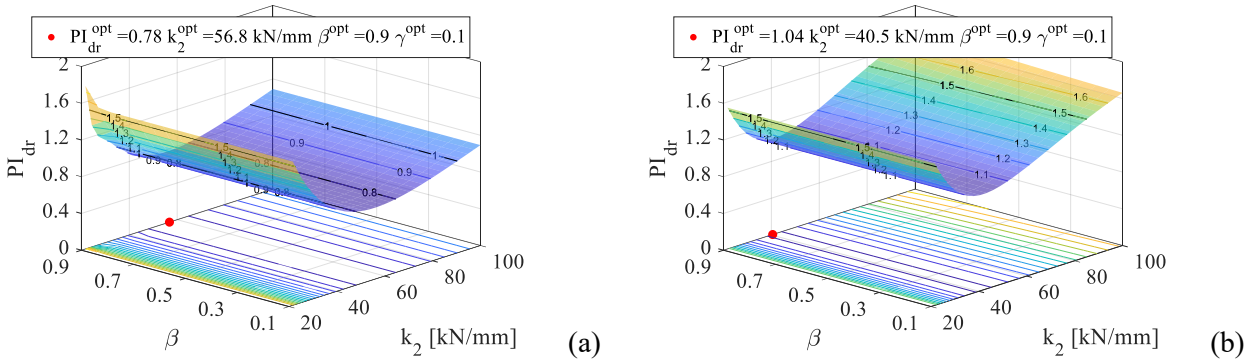

Fig. 10. Optimal surfaces in the nonlinear case: (a) one layered CMS and (b) two-layered CMS.

In order to confirm the performance of the foundation-tank coupled system with the properties provided by Fig. 10, THAs in the nonlinear regime are carried out. More precisely, k_2 values of 56.8 and 40.5 kN/mm are employed for one and two-layered foundation cases, respectively. These values entail a number of wire ropes per resonator equal to 42 and 30 for one and two-layered case, respectively, greater than those, i.e. 16 and 8, needed to bear each resonator weight.

In particular, Fig. 11 shows hysteretic loops of one wire rope -blue lines- in one-layered CMS subjected to one of the 12 natural seismic waves corresponding to a SSE in the Priolo Gargallo site. In both figures, u_{res} and u_{tl} represent displacements of the generic resonator and top-layer, respectively. More precisely, Fig. 11a refers to the optimized system in which each resonator is equipped with 42 wire ropes while Fig. 11b refers to the one in which each resonator is equipped with the minimum number of wire ropes to bear a resonator. In both cases,

β and γ read 0.9 and 0.1, respectively. One can observe that the hysteretic dampers exert a positive displacement demand of about 60 mm versus an actual experimental maximum displacement of about 10 mm shown in Fig. 9a. Therefore, an effective LRM requires a significant amount of ductility and dissipated energy for quite strong earthquakes.

Hence, given the size of the LRM, see Fig. 1b and Fig. 1c, we locate 12 and 6 dampers per resonator, for one and two-layered case, respectively. Their relevant horizontal stiffness is equal to the one provided by the aforementioned optimization procedure. THA results are shown herein only for the one-layered metafoundation case, based on Bouc-Wen parameter values collected in Table 5. In fact, as argued from Fig. 10b, the two-layered metafoundation achieves a limited performance when hysteretic dampers are used. This can also be understood from Fig. 11, where the limited performance of hysteretic dampers versus linear dampers is evident.

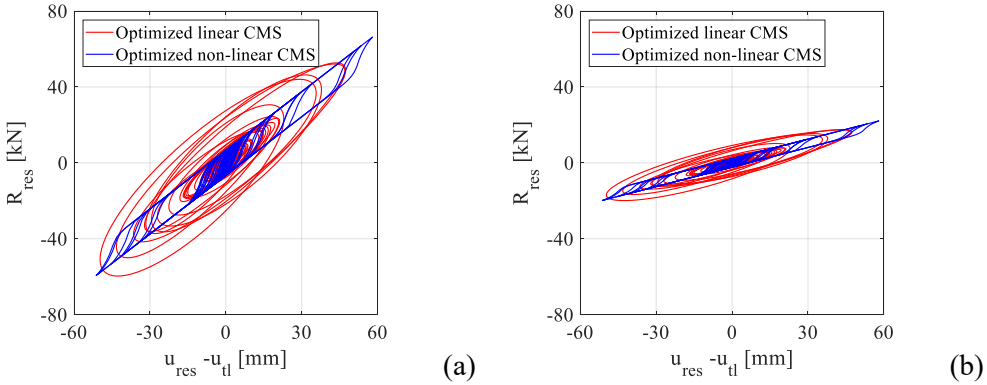

Fig. 11. Hysteretic loops of one-layered CMS hysteretic damper -blue lines, A=1, β=0.9 and γ =0.1- and linear viscous damper -red lines, $\zeta^{opt}_{1,1}$=0.2-: resonators equipped with (a) optimal and (b) minimum number of wire ropes.

Table 5
Different choices of Bouc-Wen parameters.

β = 0.9 and γ =0.1
β = 0.5 and γ =0.5
β = 0.1 and γ =0.9

Fig. 12 shows root-mean square values of the tank base shear for each considered optimal configuration: the benefits with respect to the case of a tank with a fixed foundation are evident. In agreement with the optimization outcomes, partly explained through Fig. 10a, there are no significant differences among the metafoundations equipped with wire ropes endowed with the parameters of Table 5.

An additional comparison between linear and non-linear devices entails that damping devices with a linear behavior provide more favourable results than those characterized by a hysteretic behavior. This trend is also justified by the amount of viscous and hysteretic energy wiped out. In this respect, Fig. 13 depicts the $E_d^{non\text{-}lin}/E_d^{lin}$ ratio for the one-layered CMS for each considered accelerogram. It is evident the limited performance of hysteretic dampers. Needless to say, that for the LRMs to hand endowed with resonators that move in X and Y directions, wire ropes represent a technological solution that is both much cheaper and feasible than fluid viscous dampers coupled to linear springs. Moreover, they can potentially be competitive against the vertical component of an earthquake [40].

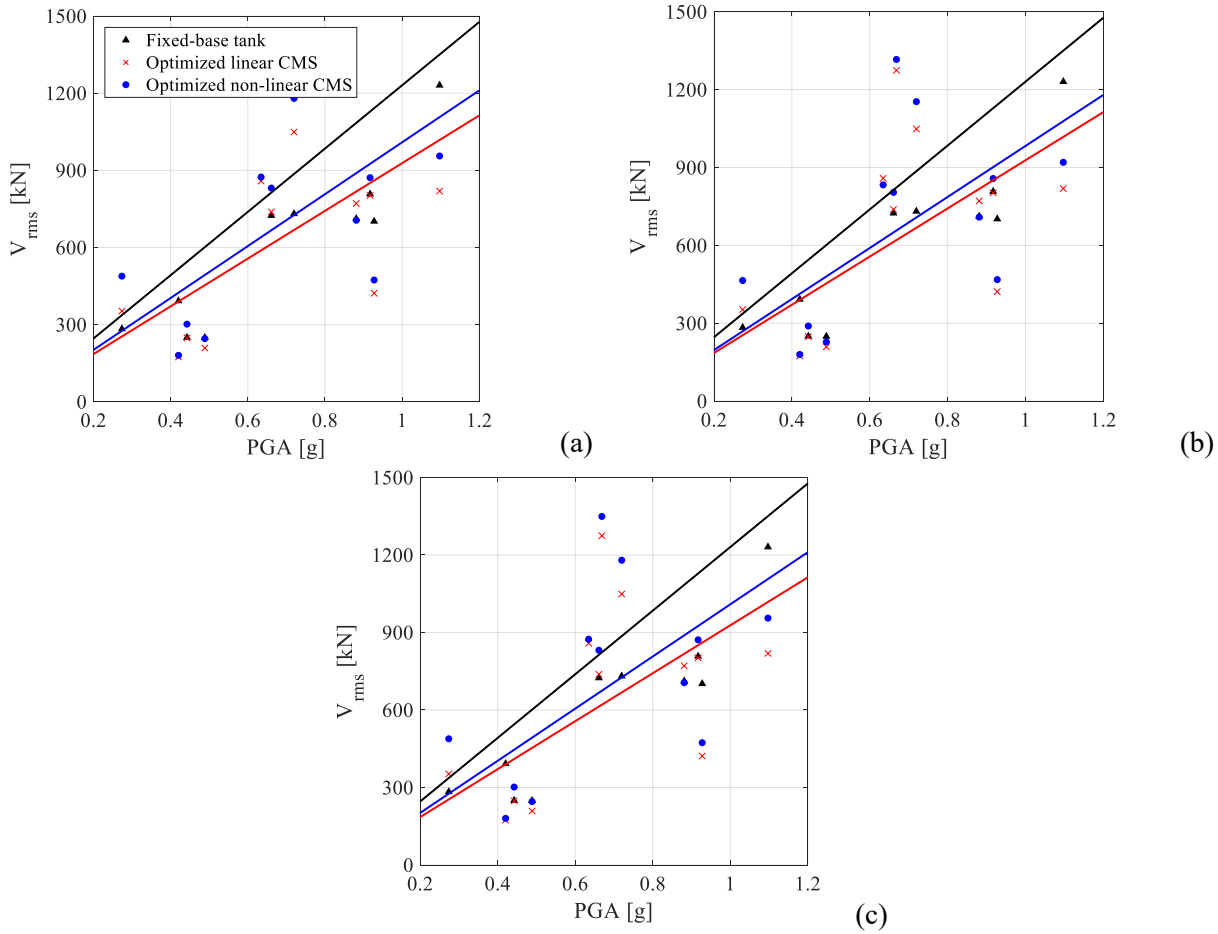

Fig. 12. Root-mean square values of the tank base shear for one-layered CMS: (a) β = 0.9 and γ =0.1, (b) β = 0.5 and γ =0.5 and (c) β = 0.1 and γ =0.9.

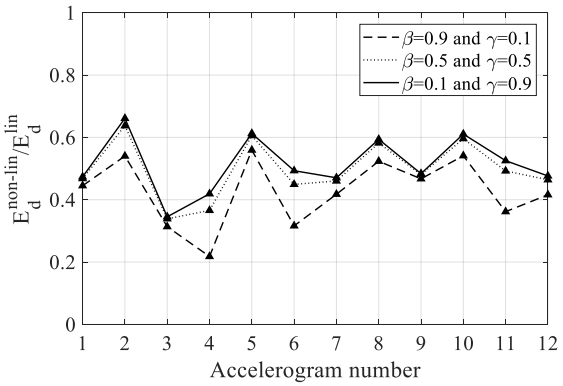

Fig. 13. $E_d^{non\text{-}lin}/E_d^{lin}$ ratio of dissipated energy by nonlinear hysteretic dampers and linear viscous dampers for the optimal cases of one-layered CMS.

6 Characteristics of the uncoupled periodic metafoundation endowed with hysteretic dampers

The performance of the finite optimized LRM depicted in Fig. 5, both with one and two layers, and endowed with fully nonlinear devices provided a favourable seismic performance of the coupled system discussed in Section 5. Therefore, given the potential vibration attenuation capabilities offered by periodic nonlinear metamaterials, it is worthy to examine the dynamic properties of the relevant uncoupled periodic metafoundation endowed with fully nonlinear devices.

6.1 Dispersion characteristics of the linearized periodic system

To crystallize the ideas, let's consider the uncoupled periodic metafoundation made of repetitive unit cells depicted in Fig. 14, endowed with nonlinear devices highlighted in Fig. 2c. For brevity, we consider the

optimized cell in which each resonator is equipped with 42 wire ropes, with $\alpha = 0.254$, $u_y = 2.2$mm, β and γ equal to 0.9 and 0.1, respectively. In addition, we assume the unit cell length $d = 1$ m and, therefore, the so-called propagation constant $\mu = \kappa d$ is equals to the wavenumber κ. Based on the ELT presented in Subsection 4.1, we naturally fall back in a linear setting where we can track mode shape families, i.e. dispersion curves, defined by means of wavelengths -or inversely, wavenumbers- and frequencies. Nonetheless, these thus derived relationships depend both on effective damping and PSD S_0.

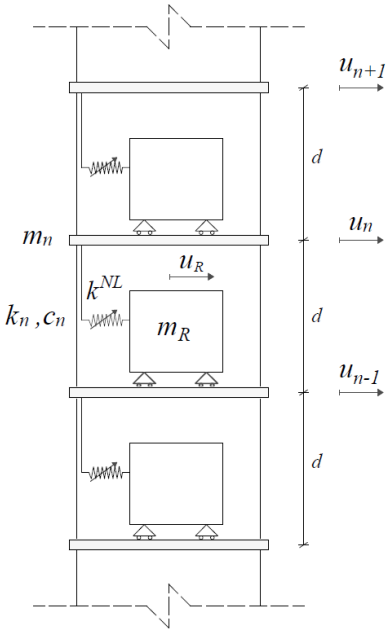

Fig. 14. Uncoupled metafoundation modelled as a periodic system

To start with, the two-DoF system associated to the unit cell, i.e. the slab and the resonator of Fig. 14, can be represented as follows,

$$\begin{cases} m_n\ddot{u}_n + c_n(\dot{u}_n - \dot{u}_{n-1}) + c_n(\dot{u}_n - \dot{u}_{n+1}) + k_n(u_n - u_{n-1}) + k_n(u_n - u_{n+1}) - \alpha k_0(u_R - u_n) - (1-\alpha)k_0 u_y z(t) = 0 \\ m_R\ddot{u}_R + \alpha k_0(u_R - u_n) + (1-\alpha)k_0 u_y z(t) = 0 \end{cases} \tag{34}$$

where dots refer to time differentiation. Spanos and Giaralis [42], among others, showed that k_{eq} and c_{eq} involved in Eq. (24) derive from a third-order ELT whose values do not correspond to any particular mechanical system; hence, their physical significance is limited. Conversely along the main vein of [42], we can rely on a second-order statistical linearization scheme, based on

$$m_R\ddot{u}_R + c_{eff}(\dot{u}_R - \dot{u}_n) + k_{eff}(u_R - u_n) = 0 \tag{35}$$

and governed by the effective linearization parameters ζ_{eff} and ω_{eff}; this leads to a clearer interpretation of dispersion curves. Along this line, we assume the following harmonic solution for displacements,

$$\begin{aligned} u_n &= \tilde{u}_n e^{i\omega t} \\ u_R &= \tilde{u}_R e^{i\omega t} \end{aligned} \tag{36}$$

being $\tilde{u}_n$ and $\tilde{u}_R$ displacement amplitudes. Besides, the Floquet-Bloch theorem can be applied as,

$$\begin{aligned} u_{n+1} &= u_n e^{i\mu} \\ u_{n-1} &= u_n e^{-i\mu} \end{aligned} \tag{37}$$

Thus, the application of the ELT by means of both third- and second-order linearization [42] together with the conditions (36) - (37), to the system of EOM (34), entails,

$$\begin{cases} \left(-\omega^2 m_n + 2i\omega c_n + 2k_n + i\omega c_{eff} + k_{eff}\right)u_n - \left(i\omega c_{eff} + k_{eff}\right)u_R - (i\omega c_n + k_n)(e^{-i\mu} + e^{i\mu})u_n = 0 \\ u_R = \dfrac{i\omega c_{eff} + k_{eff}}{-\omega^2 m_R + i\omega c_{eff} + k_{eff}} u_n \end{cases} \tag{38}$$

The replacement of u_R into the first equation of (38) leads to the following dispersion relationship,

$$\mu = \arccos\left(\frac{-\omega^2 m_n + 2i\omega c_n + 2k_n + i\omega c_{eff} + k_{eff} - \frac{\left(i\omega c_{eff} + k_{eff}\right)^2}{-\omega^2 m_R + i\omega c_{eff} + k_{eff}}}{2(i\omega c_n + k_n)} \right) \tag{39}$$

in the *(μ-ω)* plane.

Several effects due to damping endowed by linearized hysteretic devices and PSD amplitude S_0 on the dispersion relations can be understood. With regard to Fig. 15, one can notice that the acoustic curves set for the PSD amplitude $S_0 = 0.09$ m^2/s^3 point towards a center circular frequency ω_{eff} corresponding to the inelastic -hardening branch- of the Bouc-Wen model depicted in Fig. 2c. Moreover, Fig. 15 indicates that as the effective damping ratio ζ_{eff} increases, the magnitude of μ_i in the band gap zone reduces; this entails that wave attenuation becomes worse but the bandwidth zone increases. Thus, an effective damping increase in the resonators is beneficial in terms of band structure.

The effect of the nonlinearity of the resonators indirectly triggered by an increase of the PSD amplitude S_0 on the dispersion curves can be appreciated by means of Fig. 16. More precisely, one can argue that due to a general softening behaviour of hysteretic devices, larger values of S_0 entail smaller values of center circular frequencies. Finally, the impact of the nonlinearity on the position of the band structure is less significant than that of effective damping ratio ζ_{eff} illustrated in Fig. 15.

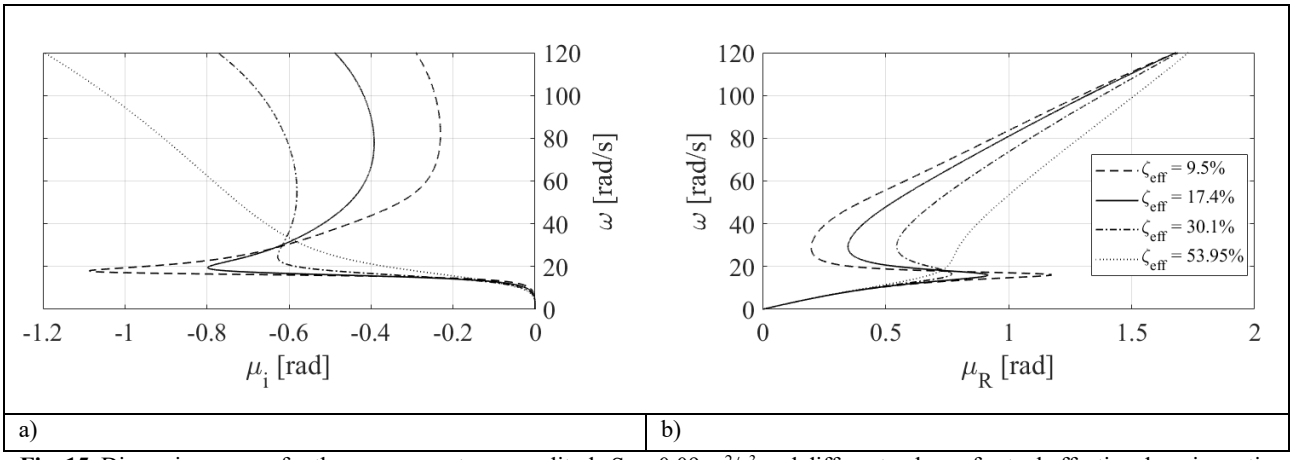

Fig. 15. Dispersion curves for the power spectrum amplitude $S_0 = 0.09$ m^2/s^3 and different values of actual effective damping ratio ζ_{eff} :(a) imaginary component of μ; (b) real component of μ

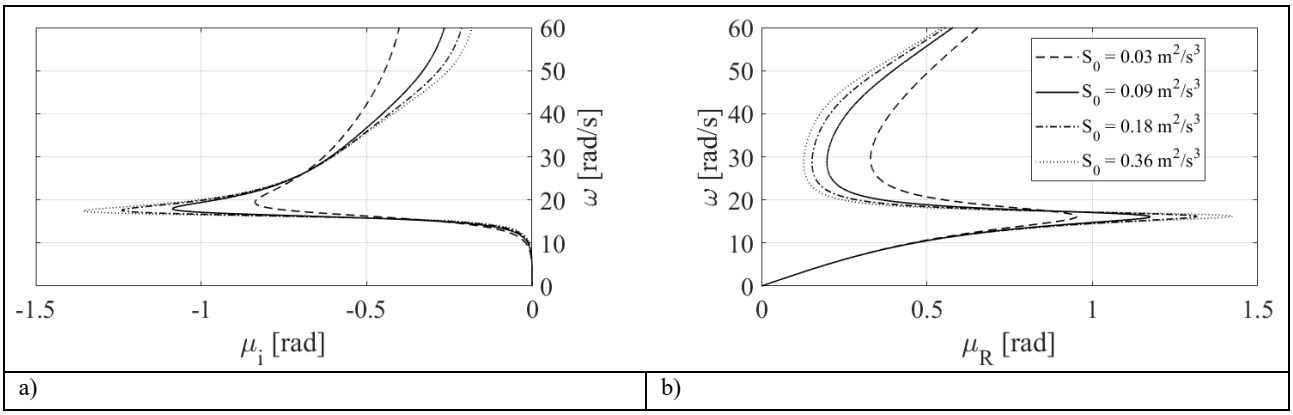

Fig. 16. Dispersion curves for initial effective damping ratio $\zeta_{eff} = 0.02$ and different values of S_0: (a) imaginary component of μ; (b) real component of μ

6.2 Dispersion characteristics of the full nonlinear hysteretic periodic system – REVISE DUE TO NEW FIGURES

In order to check the reliability of the dispersion curves presented in Subsection 6.1 based on the ELT with its variants [27, 28, 42], we carried out a numerical validation by means of transient analyses. In fact, dispersion characteristics do not reveal enough information about nonlinear wave propagation phenomena except frequency shifts. Therefore, to demonstrate other nonlinear wave propagation phenomena like wave localization or wave dispersion in nonlinear media, we employed a spectro-spatial analysis following Zhou et al. [23]. In this regard, we simulated a mass-in-mass chain consisting of 500 cells, whose parameters are equal to those used in Fig. 14. In order to omit any reflective wave, we apply perfectly match layers (PML) at each end of the chain as indicated in [26]. The chain is excited by a transient wave packet of amplitude $A_0/2$ and the velocity of each wave packet is chosen to force the wave to propagate in one direction. Typical normalized imposed wave packets defined at t = 0 sec are depicted in Figs. 18-20; the output displacement u is normalized with A_0 at t = 5 sec for different magnitudes. Simulations are conducted by numerically integrating the governing equation by the Matlab built-in solver ODE45.

After the simulation of the system at any wavenumber, we can determine the 2D Fourier transform of data in both frequency and wavenumber domains [23]. Successively, we assumed that the natural frequency of the system corresponds to the frequency associated with the point at maximum PSD. By sweeping the wave number over the first Brillouin zone, we numerically reconstructed some points of the dispersion curves from the datasets of wavenumbers and frequencies. Each of the acoustic and optimal modes was thus separately obtained by exciting the system at frequencies close to the required mode. Both the numerical and the linearized dispersion relationships corresponding to a PSD amplitude $S_0 = 0.09$ m^2/s^3 with initial effective damping $\zeta_{eff} = 0.02$ are plotted in Fig. 17 for several values of A_0.

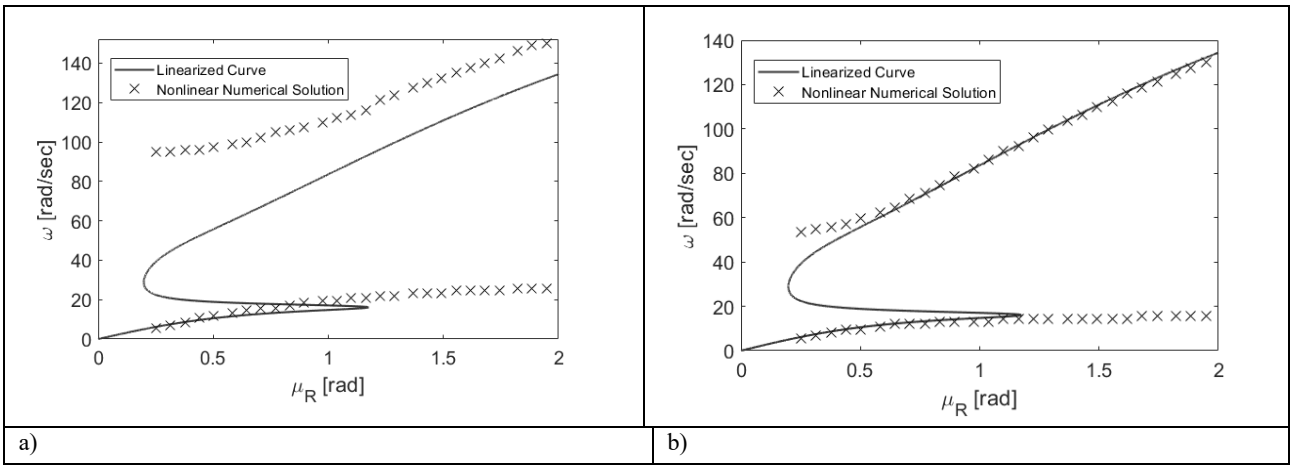

a) b)

Fig. 17. Linearized dispersion curves for a power spectrum amplitude $S_0 = 0.09$ m^2/s^3 with initial effective damping $\zeta_{eff} = 0.02$ and maximum power spectral density values based on full transient nonlinear response: (a) wave packets with low values of amplitude $A_0 = 0.01 – 0.1$ m; after Zhou et al. [23]; (b) high values of $A_0 = 0.2 – 1$ m.

Due to significant nonlinearity and damping exerted by hysteretic devices, we can trace frequencies in the low medium wavelength range with propagation constants μ_R of about 1.5. One can observe in Fig. 17(a) the actual acoustic branch and the marked frequency underestimation in the medium wavelength range caused by ELT [42]. Conversely higher values of A_0, allow for tracing frequencies pertaining to the optical mode, but the additional damping triggered by A_0 shifts down identified points of acoustic mode.

Next, we plot both the wave profile of the output response of the chain and the hysteretic response of nonlinear devices for different wave amplitudes and limits. Let's thus consider the low propagation constant $\mu_R = \frac{2}{7}\pi$ for low amplitudes in Fig. 18 and high amplitudes in Fig. 19, respectively. They clearly reveal that wave packets excites acoustic modes and that the delivered power decays, respectively less, see Fig 19, or more severely, look at Fig 20, as a function of amplitude A_0.

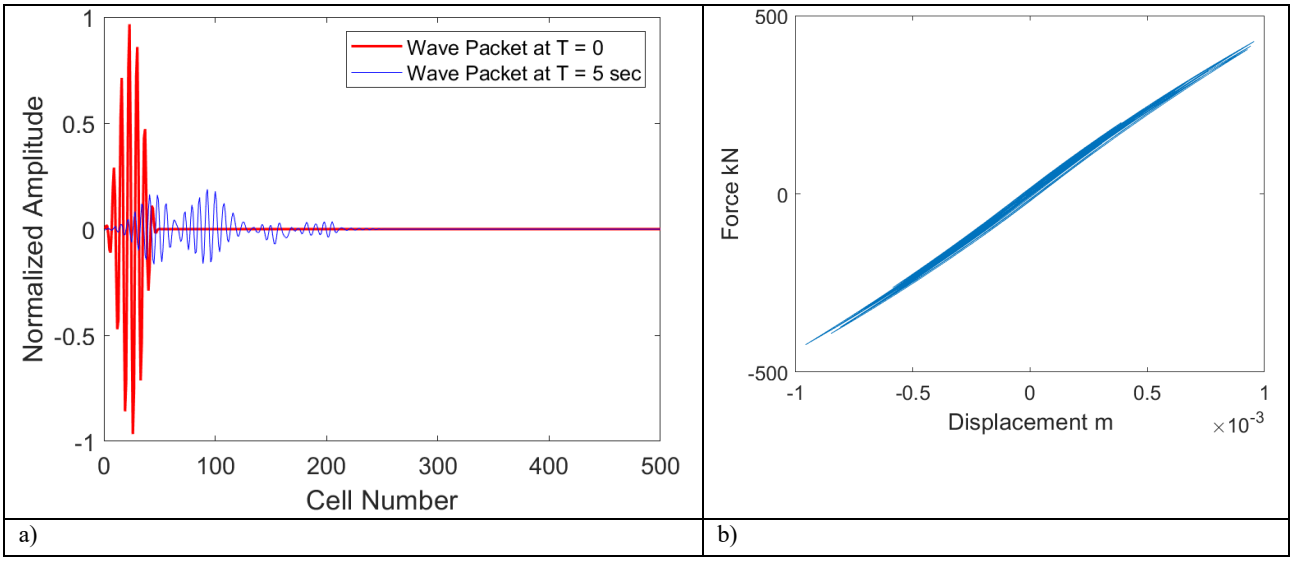

Fig. 18. Simulations relevant to the low propagation constant $\mu_R = \frac{2}{7}\pi$ for A_0 = 0.01 m: (a) spatial profile of the acoustic mode wave packet; (b) full nonlinear response of the hysteretic device

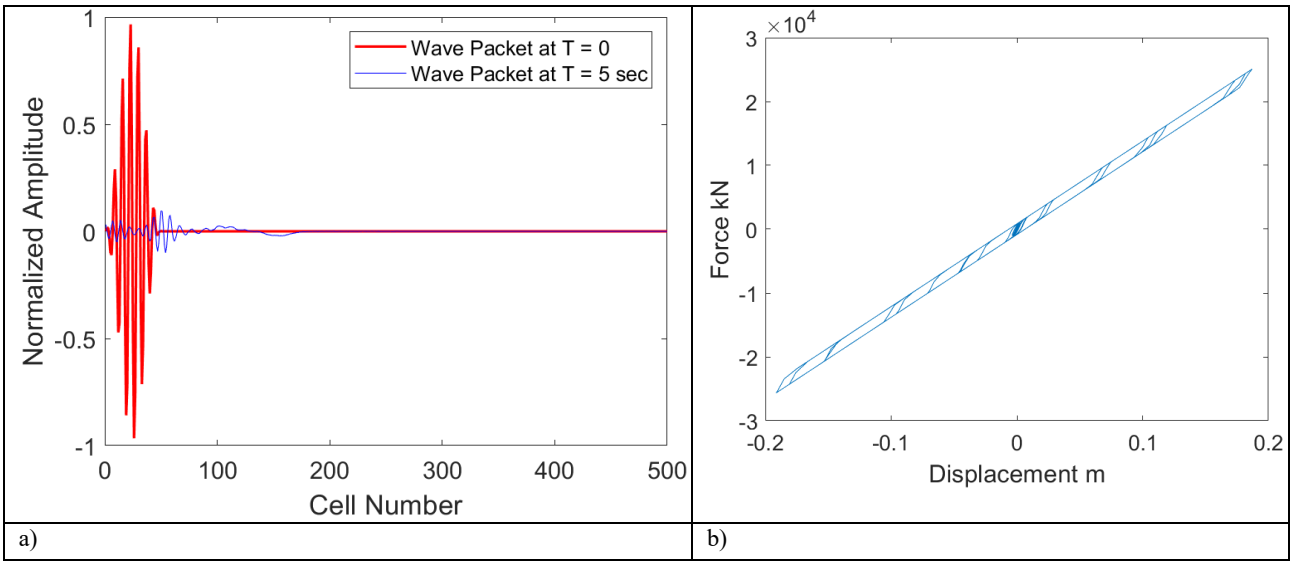

Fig. 19. Simulations relevant to the low propagation constant $\mu_R = \frac{2}{7}\pi$ for A_0 = 1.0 m: (a) spatial profile of the acoustic mode wave packet; (b) full nonlinear response of the hysteretic device

The variable slope of the dispersion curves in Fig. 17 is nonlinear and hence as expected, the waves are dispersive and relevant amplitudes significantly decrease. Moreover, waves exhibit low amplitude distributed features. The case of medium propagation constant $\mu_R = \frac{4}{9}\pi$ and optical mode is depicted in Fig. 20. Only high amplitude A_0 values are considered. Anew, the effect of dissipation entailed by the marked softening nonlinearity is significant and waves are characterized by low amplitude and dispersion; note the large hysteresis loops of Fig. 20b that indicate extensive energy dissipation. These results suggest that the interplay between high power amplitude and nonlinearity engages relatively few cells in achieving a wanted effective dispersion.

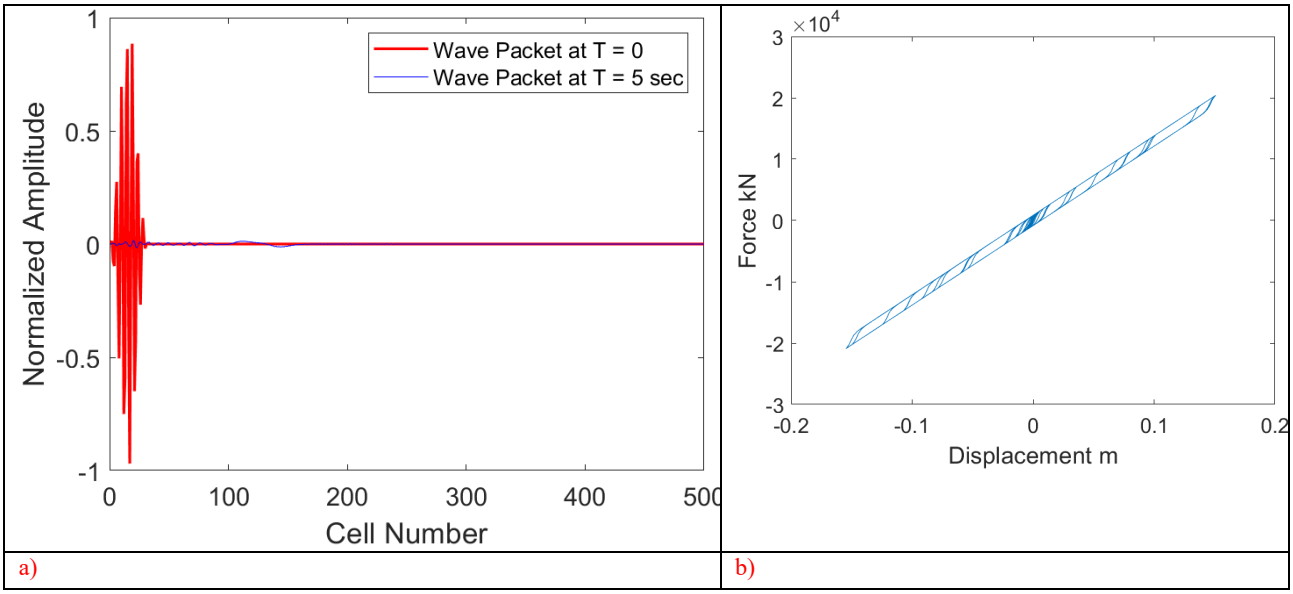

Fig. 20. Simulations relevant to the medium propagation constant $\mu_R = \frac{4}{9}\pi$ for A_0 = 1.0 m: (a) spatial profile of the optical mode wave packet; (b) full nonlinear response of the hysteretic device

7 Conclusions and future developments

In this paper, we proposed two metafoundations designed to inherit favourable properties from seismic wave propagating in finite lattice phononic structures in the ultralow-frequency regime: i) a foundation endowed with resonators and linear dampers tuned to multiple frequencies; and ii) a foundation equipped with resonators and fully nonlinear hysteretic devices. They are composed by steel-concrete composite and steel components that define exterior unit cells that contain resonating concrete masses. All configurations were characterized by one and two layers, respectively.

The tuning of this coupled tank-foundation systems was achieved through nonlinear programming in the frequency domain, which is able to optimize any number of parameters, to account for the superstructure as well as the stochastic nature of the seismic input. In particular, to optimize the nonlinear behavior of hysteretic damper devices we employed a Bouc-Wen hysteretic model; and to reduce the nonlinear differential equations of Bouc-Wen models to a system of linearized equations, we adopted the equivalent linearization technique (ELT). Then, we tested the optimized systems against natural seismic records both with linear and nonlinear time history analyses.

Optimization results showed that a locally resonant Metafoundation (LRM) with multiple resonators provides limited benefits on the structural response during earthquake events. This happened because we always considered resonators characterized by massive masses. However, the optimization procedure entailed that a system with multiple resonators allows for the reduction of optimal damping values; therefore simple linear devices can be used, however characterized by a significant amount of damping given the intensity of the seismic input. With regard to the use of nonlinear hysteretic devices, the optimization process indicated that favourable results can be achieved with simple dampers endowed with relatively high dissipative characteristics, like the wire ropes. Nonetheless, the limited performance of wire ropes with respect to the case of linear dampers in terms of dissipated energy entails a higher amount of devices in LRMs.

In order to generalize the study, we also analyzed a nonlinear mass-in-mass metastructure endowed with hysteretic devices bearing massive resonators. Anew, we employed the ELT to derive an analytical approximate solution for the spectral dispersion relationships. These expressions were validated by nonlinear transient analyses and the comparison showed that the ELT cannot predict significant frequency shift in the medium wavelength limit of the optical branch. These findings suggest that hysteretic devices needed to mitigate vibrations of superstructures subjected to strong seismic excitations alter and increase the band structure. We further investigated the nonlinear wave propagation by scrutinizing the spectro-spatial features

of the metastructure. The spatial profile of output waves both in the low and medium propagation constant demonstrated that waves are dispersive with low amplitude distributed features. *De facto*, the high value of hysteric damping strongly limits wave propagation. These results lay down the basis for future developments of LRMs, where a proper use of nonlinear hysteretic devices arranged, for instance at 45° as in Fig. 2a, requires a 3D physical characterization of the wire rope set. Finally, the optimal relation between amount of hysteretic damping, hysteretic device location also between cells and number of cells in nonlinear finite lattices, for the prediction of amplitude-dependent band structure, deserves further studies.

Acknowledgements This work received support from the European Union's Horizon 2020 research and innovation program under the Marie Skłodowska-Curie grant agreement no. 721816 for the third author and the Italian Ministry of Education, University and Research (MIUR) in the frame of the 'Departments of Excellence' (grant L 232/2016) for the remaining authors. Finally, special thanks to both Mr. F. Aloschi and Mr. T. Guner for further elaborations of Section 6.

References

[1] M.I. Hussein, M. J. Leamy, M. Ruzzene, Dynamics of Phononic Materials and Structures: Historical Origins, Recent Progress and Future Outlook, ASME Appl. Mech. Rev. 66 (2014).

[2] G. Ma, P. Sheng, Acoustic metamaterials: From local resonances to broad horizons, Science Advances 2 (2016).

[3] A. Banerjee, R. Das, E.P. Calius, Waves in Structured Mediums or Metamaterials: A Review, Archives of Computational Methods in Engineering 26 (2018) 1029-1058.

[4] Z. Liu, X. Zhang, Y. Mao, Y.Y. Zhu, Z. Yang, C.T. Chan, P. Sheng, Locally resonant sonic materials. Science 289 (2000) 1734-1736.

[5] M.V. Barnhart, X. Xu, Y. Chen, S. Shun Zhang, J. Song, G. Huang, Experimental demonstration of a dissipative multi-resonator metamaterial for broadband elastic wave attenuation, J. Sound Vib. 438 (2019) 1-12.

[6] W. Xiao, G.W. Zeng, Y.S. Cheng, Flexural vibration band gaps in a thin plate containing a periodic array of hemmed discs, Applied Acoustics 69 (2008) 255- 261.

[7] M. Maldovan, Sound and heat revolutions in phononics, Nature 503 (2013) 209-217.

[8] G. Chakraborty, A.K. Mallik, Dynamics of a weakly non-linear periodic chain. International Journal of Non-Linear Mechanics 36 (2001) 375-389.

[9] N. Menga, F. Bottiglione, G. Carbonea, The nonlinear dynamic behavior of a Rubber-Layer Roller Bearing (RLRB) for vibration isolation, J. Sound Vib. 463 (2019) 114952.

[10] S.J. Calhoun, M.H. Tehrani, P.S. Harvey Jr., On the performance of double rolling isolation systems, J. Sound Vib. 449 (2019) 330-348.

[11] V. La Salandra, M. Wenzel, O.S. Bursi, G. Carta, A.B. Movchan, Conception of a 3D metamaterial-based foundation for static and seismic protection of fuel storage tanks, Front. Mater. (2017), https://doi.org/10.3389/fmats.2017.00030.

[12] A.H. Schellenberg, A. Sarebanha, M.J. Schoettler, G. Mosqueda, G. Benzoni, S.A. Mahin, Hybrid simulation of seismic isolation systems applied to an APR-1400 nuclear power plant. PEER Report No. 2015/05 Pacific Earthquake Engineering Research Center. Headquarters at the University of California, Berkeley.

[13] O. Casablanca, G. Ventura, F. Garesc, B. Azzerboni, B. Chiaia, M. Chiappini, G. Finocchio, Seismic isolation of buildings using composite foundations based on metamaterials, J. Appl. Phys. 123 (2018) 174903, https://doi.org/10.1063/1.5018005.

[14] F. Basone, M. Wenzel, O.S. Bursi, M. Fossetti, Finite locally resonant Metafoundations for the seismic protection of fuel storage tanks, Earth. Eng. Struct. Dyn. 48 (2018) 232-252, https://doi.org/10.1002/eqe.3134

[15] G. Carta, A.B. Movchan, L.P. Argani, O.S. Bursi, Quasi-periodicity and multi-scale resonators for the reduction of seismic vibrations in fluid-solid systems, International Journal of Engineering Science 109 (2016) 216-239, https://doi.org/10.1016/j.ijengsci.2016.09.010.
[16] F. Paolacci, R. Giannini Study of the effectiveness of steel cable dampers for the seismic protection of electrical equipment. Proceedings of 14th World Conference on Earthquake Engineering October 12-17, Beijing, China (2008).
[17] S. Alessandri, R. Giannini, F. Paolacci, M. Amoretti, A. Freddo, Seismic retrofitting of an HV circuit breaker using base isolation with wire ropes. Part 1: Preliminary tests and analysis, Eng. Struct. 98 (2015) 251-262, https://doi.org/10.1016/j.engstruct.2015.03.032.
[18] P.S. Balaji, L. Moussa, M.E. Rahman, H.L. Ho, An analytical study on the static vertical stiffness of wire rope isolators, Journal of Mechanical Science and Technology 30 (2016) 287-295.
[19] Y. Wen, Method for random vibration of hysteretic systems, J. Eng. Mech. Div., Proceeding ASCE 102 (1976) 249-263.
[20] A.E. Charalampakis, V.K. Koumousis, On the response and dissipated energy of Bouc–Wen hysteretic model, Journal of Sound and Vibration (2008) 309, 887-895
[21] A. Bonelli, O.S. Bursi, Generalized-α methods for seismic structural testing, Earth. Engng. Struct. Dyn., 33 (2004) 1067-1102, https://doi.org/10.1002/eqe.390.
[22] Yousefzadeh, B., Phani, A. S. Energy transmission in finite dissipative nonlinear periodic structures from excitation within a stop band, Journal of Sound and Vibration, 354, 13, (2015), 180-195.
[23] W.J. Zhou, X.P. Li, Y.S. Wang, W.Q. Chen, G.L. Huang, Spectro-spatial analysis of wave packet propagation in nonlinear acoustic metamaterials, J. Sound Vib. 413 (2018) 250-269
[24] R. Zivieri, F. Garescì, B. Azzerboni, M. Chiappini, G. Finocchio, Nonlinear dispersion relation in anharmonic periodic mass-spring and mass-in-mass systems, J. Sound Vib. 462 (2019) 114929
[25] Sheng, P., Fang, X., Wen, J. Dianlong Yu, D., "Vibration properties and optimized design of a nonlinear acoustic metamaterial beam", Journal of Sound and Vibration 492 (2021) 115739.
[26] M. Wenzel, O.S. Bursi, I. Antoniadis, Optimal finite locally resonant metafoundations enhanced with nonlinear negative stiffness elements for seismic protection of large storage tanks, J. Sound Vib., 483, 29, 9, 2020, 115488, (2020).
[27] T.K. Caughey, Equivalent Linearization Techniques, Journal of the Acoustical Society of America 35 (1963) 1706-1711, https://doi.org/10.1121/1.1918794.
[28] L. Socha, M. Pawleta, Are statistical linearization and standard equivalent linearization the same methods in the analysis of stochastic dynamic systems?, Journal of Sound and Vibration (2001) 248(2), 387-394
[29] P.K. Malhotra, T. Wenk, M. Wieland, Simple procedure for seismic analysis of liquid-storage tanks. J Int. Assoc. Bridge Struct. Eng. 10 (2000) 197-201.
[30] K. Kanai, Semiempirical formula for the seismic characteristics of the ground, Bull. Earth. Res. Ins. 35 (1975) 309-324.
[31] R.W. Clough, J. Penzien, Dynamics of structures (1975) McGraw-Hill.
[32] NTC, CS.LL.PP. DM 17 Gennaio (2018), Aggiornamento delle "Norme tecniche per le costruzioni". Gazzetta Ufficiale della Repubblica Italiana (In Italian).
[33] G.W. Housner, The dynamic behavior of water tanks. Bull. Seismol. Soc. Am. 53 (1963).
[34] A. Kumar, S.K. Saha, V.A. Matsagar, Stochastic response analysis of elastic and inelastic systems with uncertain parameters under random impulse loading, Journal of Sound and Vibration 461 (2019) 114899.
[35] J. Kelly, Base isolation: linear theory and design. Earthq. Spectra. 6 (1990) 223-244, https://doi.org/10.1193/1.1585566.
[36] J. O'Callahan, P. Avitabile, R. Riemer, System Equivalent Reduction Expansion Process (SEREP). Proceedings of the 7th International Modal Analysis Conference, Las Vegas (1989) 29-37.
[37] O. Maldonado, M.P. Singh, F. Casciati, L. Faravelli, Stochastic response of single degree of freedom hysteretic oscillators. Technical Report of Research Supported by The National Science Foundation Under Grant Number CEE-8412830 (1987).

[38] J.B. Roberts, P.D. Spanos, Random Vibration and Statistical Linearization (1990), Wiley.
[39] R. Bartels, G.W. Stewart, Solution of the matrix equation AX + XB = C. Comm A.C.M., 15 (1972) 820-826, https://doi.org/10.1145/361573.361582.
[40] A. Franchini, O.S. Bursi, F. Basone, F. Sun, Finite locally resonant metafoundations for the protection of slender storage tanks against vertical ground accelerations, Smart Materials and Structures (2020).
[41] S. Erlicher and Bursi, O.S., Bouc-Wen-type models with stiffness degradation: thermodynamic analysis and application, Journal of Engineering Mechanics, (2008), 347, 331-338.
[42] P.D. Spanos and A. Giaralis, Third-order statistical linearization-based approach to derive equivalent linear properties of bilinear hysteretic systems for seismic response spectrum analysis, Structural Safety, 44, 59-69, 2013.

Appendix A

In this Appendix, we show how to obtain the transmission matrix $\mathrm{H}(\omega)$ for a SDoF of the Metafoundation endowed with nonlinear devices depicted in Fig. 2b and introduced in Subsection 2.3. In particular, we need to solve Eq. (24). Hence, if we consider Eq. (24) as a Cauchy problem, we obtain,

$$z(t) = -c_{eq} e^{-k_{eq}t} \left(\int e^{k_{eq}t} \dot{u}(t) dt + c \right) \tag{A.1}$$

in which *c* defines the constant of integration. The initial conditions $z(t=0)=0$ and $\dot{u}(t=0)=0$ entails *c=0*. Then, we substitute (A.1) in Eq. (5) and Eq. (6) and obtain,

$$m\ddot{u}(t) + c\dot{u}(t) + \alpha k u(t) + (1-\alpha) k u_y \left[-c_{eq} e^{-k_{eq}t} \int e^{k_{eq}t} \dot{u}(t) dt \right] = F(t) \tag{A.2}$$

The solutions $u(t) = u_0 e^{i\omega t}$ and $F(t) = F_0 e^{i\omega t}$ entail,

$$-\omega^2 u_0 e^{i\omega t} m + i\omega u_0 e^{i\omega t} c + \alpha u_0 e^{i\omega t} k + (1-\alpha) k u_y \left[-c_{eq} e^{-k_{eq}t} \int i\omega\, u_0 e^{k_{eq}t} e^{i\omega t} dt \right] = F_0 e^{i\omega t} \tag{A.3}$$

More precisely, the integral in (A.3) has the following solution,

$$\int i\omega\, u_0 e^{(i\omega + k_{eq})t} dt = \frac{i\omega}{i\omega + k_{eq}} u_0 e^{(i\omega + k_{eq})t} \tag{A.4}$$

and thus (A.3) becomes,

$$-\omega^2 u_0 e^{i\omega t} m + i\omega u_0 e^{i\omega t} c + \alpha u_0 e^{i\omega t} k - \frac{i\omega}{i\omega + k_{eq}} c_{eq} (1-\alpha) k u_y u_0 e^{i\omega t} = F_0 e^{i\omega t} \tag{A.5}$$

Eventually, the transfer function H(ω) reads,

$$\mathrm{H}(\omega) = \left[-\omega^2 m + i\omega c + \alpha k - \frac{i\omega}{i\omega + k_{eq}} c_{eq} (1-\alpha) u_y\, k \right]^{-1} \tag{A.6}$$